



University of Kentucky  
UKnowledge

---

University of Kentucky Doctoral Dissertations

Graduate School

---

2008

## MAGNETIC FIELDS IN THE GALAXY

Elizabeth Ann Mayo  
*University of Kentucky*

[Right click to open a feedback form in a new tab to let us know how this document benefits you.](#)

---

### Recommended Citation

Mayo, Elizabeth Ann, "MAGNETIC FIELDS IN THE GALAXY" (2008). *University of Kentucky Doctoral Dissertations*. 596.

[https://uknowledge.uky.edu/gradschool\\_diss/596](https://uknowledge.uky.edu/gradschool_diss/596)

This Dissertation is brought to you for free and open access by the Graduate School at UKnowledge. It has been accepted for inclusion in University of Kentucky Doctoral Dissertations by an authorized administrator of UKnowledge. For more information, please contact [UKnowledge@lsv.uky.edu](mailto:UKnowledge@lsv.uky.edu).

ABSTRACT OF DISSERTATION

Elizabeth Ann Mayo

The Graduate School

University of Kentucky

2008

# MAGNETIC FIELDS IN THE GALAXY

---

## ABSTRACT OF DISSERTATION

---

A dissertation submitted in partial fulfillment of the requirements for the degree of Doctor of Philosophy in the College of Arts and Sciences at the University of Kentucky

By  
Elizabeth Ann Mayo

Lexington, KY

Director: Doctor Thomas Troland, Professor of Physics

Lexington, KY

2008

Copyright © Elizabeth Ann Mayo 2008

## ABSTRACT OF DISSERTATION

### MAGNETIC FIELDS IN THE GALAXY

The object of this dissertation is to provide an observational study of the effects of interstellar magnetic fields on star-formation regions. This is part of a long-standing research project that uses the techniques of radio astronomy to measure magnetic field strengths in the interstellar medium of our galaxy. Interstellar magnetic fields are believed to play a crucial role in the star-formation process therefore a comprehensive study of magnetic fields is necessary in understanding the origins of stars.

These projects use observational data obtained from the Very Large Array (VLA) in Socorro, NM. The data reveal interstellar magnetic field strengths via the Zeeman effect in radio frequency spectral lines. This information provides an estimate of the magnetic energy in star-forming interstellar clouds in the Galaxy, and comparisons can be made with these energies and the energies of self-gravitation and internal motions. From these comparisons, a better understanding of the role of magnetic fields in the origins of stars will emerge. The regions observed include the giant molecular clouds and star-forming regions of Cygnus X and NGC 6334.

NGC 6334 A is a compact HII region at the center of what is believed to be a large, rotating molecular torus (based on studies by Kramer et al. (1997)). This is a continuing study based on initial measurements of the HI and OH Zeeman effect (Sarma et al. (2000)). The current study includes OH observations performed by the VLA at a higher spatial resolution than previously published data, and allows for a better analysis of the spatial variations of the magnetic field. A new model of the region is also developed based on OH opacity studies, dust continuum maps, radio spectral lines, and infrared (IR) maps.

The VLA has been used to study the Zeeman effect in the 21cm HI line seen in absorption against radio sources in the Cygnus-X region. These sources are mostly galactic nebulae or HII regions, and are bright and compact in this

region of the spectrum. HI absorption lines are strong against these regions and the VLA is capable of detecting the weak Zeeman effect within them.

KEYWORDS: Magnetic fields, Interstellar Medium,  
Star Formation, Zeeman Effect,  
HII Regions

---

Elizabeth A. Mayo

---

4/10/2008

MAGNETIC FIELDS IN THE GALAXY

By

Elizabeth Ann Mayo

---

Dr. Thomas H. Troland  
Director of Dissertation

---

Dr. Joseph Brill  
Director of Graduate Studies

---

4/10/2008

---

## RULES FOR THE USE OF DISSERTATIONS

Unpublished dissertations submitted for the Doctor's degree and deposited in the University of Kentucky Library are as a rule open for inspection, but are to be used only with due regard to the rights of the authors. Bibliographical references may be noted, but quotations or summaries of parts may be published only with the permission of the author, and with the usual scholarly acknowledgments.

Extensive copying or publication of the dissertation in whole or in part also requires the consent of the Dean of the Graduate School of the University of Kentucky.

A library that borrows this dissertation for use by its patrons is expected to secure the signature of each user.

NAME

DATE

---

---

---

---

---

---

---

---

DISSERTATION

Elizabeth Ann Mayo

The Graduate School

University of Kentucky

2008



MAGNETIC FIELDS IN THE GALAXY

---

DISSERTATION

---

A dissertation submitted in partial fulfillment of the  
requirements for the degree of Doctor of Philosophy in the  
College of Arts and Sciences  
at the University of Kentucky

By  
Elizabeth Ann Mayo

Lexington, KY

Director: Doctor Thomas Troland, Professor of Physics

Lexington, KY

2008

Copyright © Elizabeth Ann Mayo 2008

This work is dedicated to my Grandmothers, Virginia Mayo and Olive Saunders.  
Thank you for watching over me.

## ACKNOWLEDGEMENTS

There are many people I would like to acknowledge and thank for providing both insight and direction into my dissertation. To begin with I would like to thank my Dissertation Chair, Dr. Thomas Troland, not only for all of his guidance, help, and support, but also for sticking it out with me through illness and relocation. I would like to thank Anuj Sarma and Crystal Brogan for all of their help and advice on data reduction procedures. I would also like to thank my Dissertation committee, Dr. Gary Ferland, Dr. Nancy Levenson, Dr. Steven Yates, and Dr. Edward Woolery for providing thoughtful suggestions to improve the final document.

In addition there are those I would like to acknowledge who were with me through the whole process. Thanks Mom and Dad for all of your support and help, especially in the last months of all night writing sessions, month long flu, and document formatting woes. I could never have finished if you hadn't been there. Thank you to my Brothers, Steve, Dave, and Ryan and their families for believing I could do this. Thank you to my supervisor at the I.P. Stanback Museum and Planetarium, Ellen Zisholtz, for giving me the support and time to finish. Finally thank you to Shelly Leshner, my best friend and compatriot through graduate school. I couldn't have done it without you!

## TABLE OF CONTENTS

Acknowledgements .....	iii
List of Tables .....	vii
List of Figures .....	viii
List of Files .....	ix
 Chapter 1. Introduction	
1. Background.....	1
2. Basic Theoretical Concepts .....	2
2.1 Flux Freezing .....	2
2.1.1 Ambipolar Diffusion .....	3
2.2 Magnetohydrodynamic Waves .....	4
3. The Role of the Magnetic Field in Star Formation.....	5
3.1 Organization of Molecular Clouds .....	6
3.2 Mechanisms of Magnetic Support .....	6
3.3 Mass to Flux Ratio ( $M/\Phi$ ) .....	7
3.3.1 Ambipolar Diffusion Model.....	8
3.3.2 Turbulence Model.....	9
3.4 Dissipation of Angular Momentum .....	9
4. Observational Techniques .....	10
4.1 Polarization .....	10
4.1.1 Linear Polarization Techniques .....	12
4.1.2 Circular Polarization Techniques .....	13
4.2 Atomic and Molecular Zeeman Effects.....	15
4.2.1 Atomic Hydrogen (HI) .....	15
4.2.2 Hydroxyl (OH).....	16
5. Project Description.....	18
5.1 NGC 6334 A.....	18
5.2 Cygnus X.....	18
 Chapter 2. VLA Data Reduction Calibration and Editing Procedures	
1. Introduction .....	23
1.1 Radio Interferometry .....	23
1.2 The Very Large Array .....	25
1.3 Observations .....	26
2. An Overview of Calibration and Editing of VLA Data .....	27
2.1 Standard Data Calibration .....	27
2.2 Data Flagging.....	29
2.3 Self-Calibration and Maser Subtraction.....	29
3. Self-Calibration and Maser Subtraction Procedures for NGC 6334 .....	31
3.1 Preliminary Data Preparation .....	31
3.2 Self-Calibration.....	31

3.3 Maser Subtraction .....	33
3.4 Creating Stokes I and V Cubes .....	34
3.5 An Index of AIPS Tasks .....	34
Chapter 3. VLA OH Zeeman Observation of NGC 6334 A	
1. Introduction .....	36
1.1 The Zeeman Effect and Magnetic Fields .....	36
1.2 The NGC 6334 Complex .....	36
1.2.1 Source A .....	37
2. Observations and Data Reduction .....	38
2.1 Observations .....	38
2.2 Data Reduction .....	38
2.2.1 An Attempt to Remove Maser Contamination .....	38
3. Results .....	39
3.1 Continuum Emission .....	39
3.2 OH Line Data .....	40
3.2.1 Optical Depths and Column Densities .....	40
3.2.2 Kinematics of the OH Gas .....	42
3.2.3 1667/1665 MHz OH Line Ratios .....	42
3.3 Magnetic Field Determination .....	43
3.3.1 Spatial Variations of Magnetic Fields Toward NGC 6334 A .....	44
4. Discussion .....	45
4.1 The Nature of NGC 6334 A and its Lobes .....	45
4.1.1 Molecular Gas in the NGC 6334 A Region .....	45
4.1.2 The Central Shell .....	48
4.1.3 The Nature of the Central Exciting Source .....	49
4.1.4 The Northern Lobe .....	50
4.1.5 The Southern Lobe of Radio Continuum Emission .....	51
4.1.6 A Model for the NGC 6334 A Region .....	52
4.2 Magnetic Effects in the NGC 6334 A Region .....	54
Chapter 4. VLA HI Zeeman Observations of the Cygnus X Regions, DR 22 and ON 2	
1. Introduction .....	71
1.1 The Cygnus X Star Forming Region .....	71
2. Observations and Data Reduction .....	72
3. Results .....	72
3.1 Continuum .....	72
3.1.1 DR 22 .....	72
3.1.2 ON 2 .....	72
3.2 HI Line Data .....	73
3.2.1 DR 22 .....	73
3.2.2 ON 2 .....	74
3.3 Magnetic Fields .....	74
3.3.1 DR 22 .....	74

4. Discussion .....	75
4.1 ON 2.....	75
4.1.1 The Determination of the Central Ionizing Source from Radio Continuum Flux .....	75
4.2 DR 22.....	76
4.2.1 Molecular Line Observations of the DR 22 Star-Forming Region .....	76
4.2.2 Infrared Observations of the DR 22 Star-Forming Region .....	76
4.2.3 Radio Observations of the DR 22 Star-Forming Region .....	77
4.2.4 Calculation of Total Hydrogen Column Density for the DR 22 Core Region .....	78
4.2.5 Magnetic Support and Virial Estimates for the DR 22 Core Region .....	79
 Chapter 5. Discussion and Conclusions	
1. Summary of Results.....	94
1.1 NGC 6334 A.....	94
1.1.1 A New Model .....	94
1.1.2 Magnetic Effects.....	94
1.2 Cygnus X.....	95
1.2.1 ON 2.....	95
1.2.2 DR 22 .....	95
2. Magnetic Fields in Molecular Clouds .....	96
2.1 Comparison to Crutcher (1999).....	96
2.2 Conclusions.....	97
 References .....	100
 Vita .....	105

## LIST OF TABLES

Table 3.1, Observational Parameters for VLA Observations .....	58
Table 3.2, NGC 6334 A Parameters .....	59
Table 4.1, Observational Parameters for VLA Observations .....	81
Table 4.2, Derived Exciting Stars for ON 2 Region.....	82
Table 4.3, DR 22 Parameters .....	83
Table 4.4, DR 22 Derived Values and Virial Estimates.....	84
Table 5.1, Magnetically Significant Parameters.....	99

## LIST OF FIGURES

Figure 1.1, Estimating the Magnetic Field Strength .....	20
Figure 1.2, Ground State of HI in the Presence of a Magnetic Field.....	21
Figure 1.3, Ground State of OH in the Presence of a Magnetic Field .....	22
Figure 3.1, 18 cm Continuum Map of the NGC 6334 Complex at 1667 MHz ....	60
Figure 3.2, 18 cm Continuum Map of NGC 6334 A at 1667 MHz.....	61
Figure 3.3, Uniformly Weighted 18 cm Continuum Map of NGC 6334 A at 1667 MHz.....	62
Figure 3.4a, OH Optical Depth Profile toward the Northern Lobe of NGC 6334 A .....	63
Figure 3.4b, Optical Depth Profile toward the Core of NGC 6334 A .....	63
Figure 3.4c, Optical Depth Profile toward the Southern Lobe of NGC 6334 A ...	63
Figure 3.5, Plot of $N(\text{OH})/T_{\text{ex}}$ toward NGC 6334 A with 1667 MHz Continuum Contours .....	64
Figure 3.6a, Stokes I and V Profiles in the OH 1665 MHz Line Toward NGC 6334 A.....	65
Figure 3.6b, Stokes I and V Profiles in the OH 1667 MHz Line Toward NGC 6334 A.....	65
Figure 3.7, Map of Magnetic Field Strengths toward NGC 6334 A with 1667 MHz Continuum Contours .....	66
Figure 3.8, Integrated SiO Line with 850 $\mu\text{m}$ Dust Emission Contours.....	67
Figure 3.9, 850 $\mu\text{m}$ Dust Emission with 1667 MHz Radio Continuum Emission.	68
Figure 3.10. 1667 MHz Continuum Emission with 3.3 $\mu\text{m}$ PAH Image.....	69
Figure 3.11, Model of NGC 6334 A Region .....	70
Figure 4.1, 21 cm Continuum Map of DR 22 at 1420 MHz .....	85
Figure 4.2, 21 cm Continuum Map of ON 2 at 1420 MHz.....	86
Figure 4.3, 21 cm Continuum Map of ON 2 at 1420 MHz.....	87
Figure 4.4, HI 1420 MHz Optical Depth Profile toward the Core of DR 22 .....	88
Figure 4.5, Plot of $N(\text{HI})/T_{\text{ex}}$ toward DR 22 with 1420 MHz Continuum Contours .....	89
Figure 4.6, Plot of $N(\text{HI})/T_{\text{ex}}$ toward DR 22 with 1420 MHz Continuum Contours Summed Across the -7 km/s Component.....	90
Figure 4.7a, 1420 MHz Optical Depth Profile Toward ON 2 N.....	91
Figure 4.7b, 1420 MHz Optical Depth Profile Toward ON 2 NE .....	91
Figure 4.7c, 1420 MHz Optical Depth Profile Toward ON 2 S.....	91
Figure 4.8a, Stokes I Profile in the 1420 MHz HI Line Toward DR 22 .....	92
Figure 4.8b, Stokes V Profile in the 1420 MHz HI Line toward DR 22.....	92
Figure 4.9, K-Band Image of DR 22 from 2MASS with 1420 MHz Continuum Contours .....	93



## LIST OF FILES

EMayo\_Dissertation.pdf 1.42 MB

# Chapter 1. Introduction

## 1. Background

In the 1983 edition of *Scientific America*, E.N. Parker described the interstellar magnetic field as the “Cosmic Agitator,” and stated that without this field the “cosmos would resemble the serene and monotonous heavens of classical conception.” Indeed, magnetic fields are responsible for all kinds of astrophysical phenomena: from the earthly auroral displays, to stellar flares, to the dynamics of the interstellar medium and star formation. The latter topic is the focus of this thesis.

The basic idea of star formation is well understood although there are several problems. If the internal pressures in clouds of interstellar material are too low for support, the material will be drawn together by self-gravity. In such a manner diffuse, cold interstellar clouds organize themselves into the denser, more compact regions from which stars are born. The study of the role of the magnetic field in these regions addresses two basic problems inherent in the process. First is the problem of star-formation rate. Gas in the galaxy should be gravitationally unstable, converting its mass into stars on a free-fall time scale. However, if this were the case, star formation rates would be three orders of magnitude higher than what is observed in the galaxy today ( $3M_{\text{sun}}/\text{yr}$ , McKee 1999). Obviously there is something inhibiting the formation of stars in such regions, and magnetic pressure is a possibility. Second is the problem of angular momentum. In order to form stars, interstellar clouds must find a means to dissipate angular momentum. For example, a 2 solar mass fragment of interstellar material at average density of  $1 \text{ cm}^{-3}$  possesses angular momentum  $\approx 10^{55} \text{ g cm}^2 \text{ s}^{-1}$  from galactic differential rotation alone. Yet a wide binary star system of the same mass possesses two orders of magnitude less angular momentum, and the Sun (including the orbital motion of Jupiter) has four orders of magnitude less angular momentum (Mouschovias 1987). An obvious mechanism for removal of angular momentum from a star-forming cloud is the hydromagnetic waves generated by a rotating interstellar cloud with frozen-in magnetic fields (see §3.4 below).

In the following discussion, the role of the magnetic field in the dynamics of interstellar material is discussed, emphasizing the importance of the magnetic field in regions of star formation. Based on this material, the projects described will make great strides toward answering the questions described above.

## **2. Basic Theoretical Concepts**

### **2.1 Flux Freezing**

When considering the role the magnetic field plays in the dynamics of the interstellar material, we consider the interaction between matter and the magnetic field. Charged particles immersed in a magnetic field will experience the Lorentz Force,  $\mathbf{F} = q\mathbf{v} \times \mathbf{B}$ , where  $\mathbf{F}$  is defined as the force experienced by a particle of charge  $q$  moving with a velocity  $\mathbf{v}$  in a magnetic field of strength  $\mathbf{B}$ . The Lorentz force causes the particles to spiral around the magnetic field, coupling the field and the charged particles. The ionized particles are said to be “frozen” to the magnetic field. That is, we have a self-consistent system in which the helical motion of the charged particles is determined by the magnetic field, and the electric current represented by the moving charges sustains the magnetic field. The only way a charged particle can escape from the field lines is through collisions with other charged particles. Collisions between charged particles provide an electrical resistance that dissipates particle motions and the energy of the magnetic field (ohmic dissipation). Ohmic dissipation occurs due to collisions between ions. These collisions dissipate the motions of the charged particles, converting electrical energy into other types of energy such as heat. Therefore, frequent collisions tend to prevent the freezing of particles to the field lines and, also, destroy the magnetic field. In a dense gas (e.g. the Earth’s atmosphere at sea level), collisions are very frequent, so the field would dissipate rapidly. However, in the ultra low density interstellar environment ( $10^0 - 10^4$  particles  $\text{cm}^{-3}$ ), collisions are rare. So charged particles are very effectively bound to the field lines, and the dissipation timescale of the magnetic field is extremely long. The time scale for a significant change in field strength via ohmic dissipation is of order  $4\pi L/\eta$ , where  $L$  is the size scale of the field and  $\eta$  is the

electrical resistivity in emu (Spitzer 1978). Since  $\eta$  is very low in the ISM, the timescale is long, approximately  $10^9$  years even if  $L$  is as small as 1 AU.

To illustrate the close coupling of charged particles to the magnetic field, consider a proton moving at a thermal velocity characteristic of the ISM at 100 K (2 km/s), placed in a magnetic field of  $10^{-6}$  G (a typical magnetic field strength for the interstellar medium.) The gyroradius of this proton is  $2 \times 10^3$  km, an insignificantly small distance on an astronomical scale.

In the interstellar medium, charged particles are closely coupled to the magnetic field via the mechanism described above. At the same time, neutral particles are coupled to the charged particles by collisions. Therefore even largely neutral gas is well coupled to the field, a mechanism known as flux freezing. Flux freezing has many consequences in the star formation process.

Flux freezing is dependent upon the presence of ions in regions of the ISM. Thus, the density of free electrons with respect to neutral hydrogen ( $n_i/n_H$ ) or fractional ionization becomes important in such regions. With the exception of HII regions where the fractional ionization is 1 (100% ionized), by mass the ISM is overwhelmingly neutral. Throughout most of the neutral ISM, ionization is due to starlight, and the free electrons come mainly from singly ionized carbon  $C^+$ , the most abundant element with an ionization potential (11.26 eV) less than that of hydrogen. The fractional ionization in this neutral medium is  $n_i/n_H \sim 5 \times 10^{-4}$  (Spitzer 1978). Ionization due to starlight is excluded in dense molecular cores and the free electrons come from ionization of hydrogen due to cosmic-rays. The low fractional ionization ( $n_i/n_H \sim 10^{-7}$ ) within the molecular core allows for the slow leakage of magnetic flux from the neutral material (Spitzer 1978)(Crutcher et al. 2003 ). This process is called ambipolar diffusion and allows for molecular cloud evolution (Shu et al 1987). Ambipolar diffusion is described in detail in §2.1.1.

### **2.1.1 Ambipolar Diffusion**

As outlined above, the magnetic field in a cloud core affects only the charged particles directly; the neutral particles are coupled only through ion-neutral collisions. If the fractional ionization is low (as in dense molecular cores) flux freezing can break down. As the cloud contracts, the neutral particles are

propelled by gravity to the center of the core while the charged particles are left behind, attached to the magnetic field lines. This slow drift of neutral particles into the core center without a significant increase in the magnetic flux is known as ambipolar diffusion (APD). Eventually, the central core mass will become so large that the magnetic field threaded through it can no longer support the core and gravitational collapse will ensue. In this way, star formation can proceed in cores which were originally supported by the magnetic field. The fundamental parameter that is used to describe the role of the magnetic field in a molecular core is the mass-to-flux ratio. This is a measure of the ratio of gravitational to magnetic energies, and is fully described in §3.3.

In typical interstellar conditions, the time scale for ambipolar diffusion exceeds the time scale for free-fall collapse. The approximate time scale for ambipolar diffusion is given by:

$$t_{AD}=5.0 \times 10^{13} n_i/n_H \text{ years (Spitzer 1978)}$$

where  $n_i/n_H$  is the ratio of positive ion density to overall hydrogen density. For a relatively dense cloud  $n_H \approx 10^6 \text{ cm}^{-3}$ ,  $n_i/n_H \approx 10^{-7}$  and  $t_{AD} = 5 \times 10^6$  years. The free-fall time scale is  $t_f = 4 \times 10^4$  years, where the free-fall time is defined as:

$$t_f = 4.3 \times 10^7 / n_H^{1/2}$$

It is the process with the longest time scale that drives the evolution of a cloud. Therefore, the ambipolar diffusion process controls the evolution of clouds or cores that are supported by the magnetic field through flux-freezing. However, the neutral medium has a fractional ionization of  $n_i/n_H \sim 5 \times 10^{-4}$  giving  $t_{ad} = 3 \times 10^{10}$  years, too long a time to be of interest in interstellar conditions (Spitzer 1978). Thus ambipolar diffusion is also dependent upon the fractional ionization of the regions studied, and it is expected to be important only in those regions shielded from ionizing starlight, that is, the cores of molecular clouds where star-formation occurs.

## 2.2 Magnetohydrodynamic (MHD) Waves

Closely related to the concept of flux freezing is the generation of MHD waves in the interstellar medium. Due to the freezing of magnetic flux into interstellar material, fluctuations of the magnetic field or MHD waves give rise to

macroscopic motions within the cloud (and vice versa), which in turn can provide support for the cloud. MHD waves are also believed to be a critical component of angular momentum dissipation through magnetic-braking (see §3.4) in the star formation process. Phenomena that give rise to MHD waves are cloud collisions, stellar wind, and shocks since they introduce mechanical energy into the ISM coupled to the field.

MHD waves in the interstellar medium have several modes. Most relevant to the work discussed in this thesis is the Alfvén wave and speed, which has implications for the strength of the magnetic field in dense molecular clouds. This mode of MHD wave is a transverse wave that propagates parallel to the mean field at the Alfvén speed  $V_A$ . Particle motions are perpendicular to the propagation direction. The Alfvén speed,  $V_A$  is defined as:

$$V_A = |B| / (4\pi\rho)^{1/2},$$

where  $|B|$  is the magnetic field strength and  $\rho$  is the gas density within the cloud. Using observations of the magnetic field strengths and gas densities within the clouds, it is possible to estimate the Alfvén speed in a cloud.

The width of a spectral line is composed of a thermal contribution due to the microscopic motions of the individual gas particles and a non-thermal contribution due to semi- or disorganized macroscopic (turbulent) motions in the cloud. Turbulence, along with thermal motions, acts as a type of pressure in interstellar clouds. Observations of the line widths in the ISM usually reveal a substantial non-thermal contribution indicating that the turbulence is supersonic. Supersonic turbulence can be generated in many ways such as supernovae, stellar winds, and cloud-cloud collisions. If the observed non-thermal contribution to the line width of a spectral line is about equal to the estimated Alfvén speed, then it is possible that the turbulent motions in the cloud are Alfvén waves.

### **3. The Role of the Magnetic Field in Star Formation**

There are two competing ideas for the processes driving star formation. The first view is that self-gravitating clouds are supported against collapse by the magnetic field, with ambipolar diffusion reducing the support of the cores until gravitational collapse occurs and stars are formed (§2.1.1). The competing idea

relies on compressible turbulence to form and disperse molecular clouds in the interstellar medium. Supersonic turbulence leads to shock waves that heat the ISM. The heated ISM radiates more efficiently, dispersing the energy that was once kinetic energy in the cloud. When the turbulence disperses, the clouds that become gravitationally bound will eventually collapse and form stars. This latter process effectively makes the question of long-term support for molecular clouds irrelevant. The study of the magnetic field is obviously very important for a complete understanding of the star formation process. Below are discussed the principle mechanisms of magnetic support in molecular clouds.

### **3.1 Organization of Molecular Clouds**

All known star formation takes place in molecular clouds, the majority taking place in structures known as Giant Molecular Clouds (GMCs). GMCs are self-gravitating molecular clouds with masses greater than  $10^4$  solar masses. By mass, these clouds, along with globular clusters, are the largest known individual objects in the galaxy.

GMCs themselves contain denser regions of material, known as cores, that have a coherent velocity and are separated from other cores both spatially and in velocity. Star formation takes place in the most tightly gravitationally bound cores, and within these only in the densest region in the central parts.

### **3.2 Mechanisms of Magnetic Support**

The magnetic field in a cloud can be described in terms of a static or uniform component and a time-dependent wave or random component:

The static component threads both the cloud and the external medium and determines the total magnetic flux through the cloud. The static field component may also provide major support for the denser regions of molecular clouds against self-gravity. This mechanism of support is known as magnetic pressure, and it augments the thermal pressure in support of the cloud as well as the pressure associated with turbulent motions.

When interstellar material begins its collapse into dense molecular clouds and eventually stars, the magnetic field lines are effectively frozen into the matter through the coupling with the charged particles and through these, neutral

particles. When the cloud contracts, the magnetic field lines must move with the cloud and are compressed, increasing the strength of the magnetic field within. Analogous to a rubber band, after the cloud has contracted the magnetic field exerts a force that tries to return the cloud back to its previous configuration. This force prevents further contraction; however, it only provides support perpendicular to the magnetic field lines.

The wave component of the magnetic field is closely associated with the MHD waves described above. Because the magnetic field is connected to the general medium, supernova explosions or shocks for example can transfer energy along the magnetic field lines, effectively perturbing the field. This will provide 3-D support through turbulent motions within the cloud.

### **3.3 Mass to Flux Ratio ( $M/\Phi$ )**

The fundamental parameter when determining the role of the magnetic field in a molecular cloud core is the mass-to-flux ratio. Strictly speaking, this ratio reflects the amount of cloud mass lying along a given magnetic flux tube, and the ratio could be a function of position in the cloud. More approximately, the ratio is a measure of gravitational to magnetic energies; that is, the approximate ratio of  $GM^2/R$  to  $(4/3)\pi R^3 \times B^2/8\pi$  where  $R$  is the radius of a cloud,  $M$  is the mass and  $B^2/8\pi$  is the magnetic energy density, with  $B$  the magnetic field strength. A critical mass-to-flux ratio where the gravitational and magnetic energies are equal can be defined as

$$(M/\Phi)_{\text{crit}} = C_\Phi / G^{1/2},$$

where  $C_\Phi$  is a constant of order unity and is dependent on the shape of the cloud and  $G$  is the gravitational constant (Mouschovious and Spitzer 1976). From this quantity the parameter  $\lambda$  is defined as:

$$\lambda = (M/\Phi) / (M/\Phi)_{\text{crit}}$$

where  $\lambda$  remains constant during core evolution as long as flux freezing is maintained. The mass-to-flux ratio is analogous to the Chandrasekhar limit for white dwarf stars. In much the same way that electron degeneracy pressure will resist the transformation of a white dwarf to a neutron star, frozen in magnetic



flux will resist the transformation of molecular clouds into stars when  $\lambda < 1$  (Shu et al 1987).

For  $\lambda > 1$  the magnetic field alone cannot prevent gravitational collapse, and the cloud core is magnetically supercritical. In the absence of other mechanisms of support, in particular, internal motions, a magnetically supercritical core must collapse. For  $\lambda < 1$  the magnetic field prevents gravitational collapse and the cloud is magnetically subcritical. A magnetically subcritical core can never form stars as long as flux freezing is maintained. However, the central regions of a magnetically subcritical cloud can become magnetically supercritical through the process of ambipolar diffusion (§2.1.1).

### **3.3.1 Ambipolar Diffusion Model**

In the ambipolar diffusion model clouds are initially subcritical ( $\lambda < 1$ ). In high density cores that are shielded from starlight (where the fractional ionization is low), ambipolar diffusion proceeds rapidly. The cores eventually become supercritical and collapse. The envelopes of these cores continue to be supported by the magnetic field and are thus magnetically subcritical (Paleologou and Mouschovias, 1983 and §2.1.1).

Clouds undergoing ambipolar diffusion will exhibit specific morphologies and magnetic field strengths. The magnetic field would be sufficiently strong that  $\lambda \leq 1$ , with smooth magnetic field lines not dominated by irregular structure. Clouds would be thin disks or oblate spheroids, since thermal and turbulent pressure provide the only support parallel to the field lines. The field lines would then lie parallel to the minor axis of the cloud. As the disk contracts perpendicular to the field lines (due to ambipolar diffusion), the field lines connecting the cloud to the medium would take on an hourglass morphology where the tension in the bent field lines provides the support (Crutcher et al. 2003).

The ambipolar diffusion model predicts a relationship between the magnetic field strength and the volume density of gas such that  $B \propto \rho^k$  where  $k$  for the core is small ( $\sim 0.1-0.2$ ) in the early stages of evolution. Once the core becomes magnetically supercritical and collapses, the magnetic field is dragged

in with the material and increases with  $k \sim 0.4$  approaching 0.5 (Crutcher et al. 2003). In the envelope, where the ambipolar time scales are much longer owing to the higher fractional ionization,  $B$  remains unchanged. Therefore, there is no expected correlation between  $B$  and  $\rho$  in the envelopes surrounding the cores.

Thus we can test our observations against the predicted morphologies, magnetic field strengths, and mass-to-flux ratios within the cloud. For example, one way to test the ambipolar diffusion model would be to measure the mass-to-flux ratios of the envelopes surrounding the collapsing supercritical cores. They should be magnetically subcritical if the ambipolar diffusion model applies.

### **3.3.2 Turbulence Model**

The turbulence model suggests that clouds formed by compressible turbulence must be magnetically supercritical as the magnetic field is insufficient to prevent the collapse of the cloud. Thus  $\lambda$  can take any value greater than 1 (Crutcher et al. 2003).

In the turbulent model, the magnetic energy is much less than the turbulent energy, thus the field lines would be chaotic with random small-scale structure (Crutcher 1999). The turbulent model predicts no correlation between the volume density of the gas and the magnetic field strength for the low density case where gravity is unimportant. Once the clouds become gravitationally bound, a rough equipartition of energy is achieved. By assuming virial equilibrium between gravity, turbulence, and flux freezing one can predict  $B \propto \Delta v \rho^2$  where  $\Delta v$  is the line width. In comparison with the ambipolar diffusion model, we find that both models predict  $k=0.5$  with an extra dependence on the line width predicted in the turbulence model (Crutcher et al. 2003).

### **3.4 Dissipation of Angular Momentum**

The angular momentum of a molecular core will act to prevent collapse to a small radius. Therefore, there must be a way to dissipate the angular momentum as the cloud collapses to form a star. It was first suggested by Mestel and Spitzer (1956) that the magnetic field plays an important role in the dissipation of angular momentum from a contracting interstellar cloud into the surrounding medium. The mechanism is as follows: the magnetic field lines that

thread through both the interstellar medium and the cloud are frozen into the material. The flux freezing of the field lines causes them to twist in the cloud as the cloud rotates relative to the surrounding medium, producing a tension in the magnetic field lines. The tension imparts a force that sets the surrounding gas into motion, corotating with the cloud. Setting the surrounding medium into motion removes angular momentum from the cloud. In terms of magnetohydrodynamics, the tension in the twisted field lines within the clouds generates MHD waves that carry away angular momentum. This phenomenon is called magnetic braking.

## **4 Observational Techniques**

### **4.1 Polarization**

In 1949 Hiltner and Hall observed the phenomenon of starlight polarization. It was soon noted that adjacent stars have similar orientations of their linear polarizations, indicating the presence of a large-scale interstellar magnetic field. The polarization of starlight is attributed to elongated, spinning dust grains in the ISM aligned by the magnetic field. This phenomenon has become an important observational tool in the study of magnetic fields (§4.1.1).

Virtually all of the techniques used today to study interstellar magnetic fields rely upon the detection of polarized radiation passing through or emitted by the interstellar medium. These techniques can be divided into two complementary types: techniques utilizing linear polarization and those utilizing circular polarization. Linear polarization methods such as dust grain alignment and synchrotron radiation emission provide useful information on the *orientation* of magnetic fields on the plane of the sky but yield little information on magnetic field *strengths*. These methods have been used to map the direction on the plane of the sky of the large scale Galactic magnetic field (Heiles 2000a). To complement these studies, through the detection of circularly polarized radiation, the Zeeman effect in radio frequency spectral lines can be utilized to make measurements of the strengths of the magnetic field.

The polarization of radiation is described in terms of the Stokes Parameters: I, Q, U, V. Stokes parameter I describes the total intensity of

radiation, Q and U describe the linear polarization of radiation, and V the circular polarization. Following the formulation of Crutcher et al. (1993), we define the quantity T to represent the power per unit bandwidth received by a radio telescope with a receiver sensitive to a single state of circular or linear polarization. We define  $\phi$  as the position angle of the component of  $\mathbf{B}$  in the plane of the sky. Then we can define the Stokes parameters as:

$$I = T_r + T_l$$

$$V = T_r - T_l$$

$$Q = (T_{\parallel} \cos \phi + T_{\perp} \sin \phi) - (T_{\parallel} \sin \phi + T_{\perp} \cos \phi)$$

$$U = [T_{\parallel} \cos(45^\circ - \phi) + T_{\perp} \sin(45^\circ - \phi)] - [T_{\parallel} \sin(45^\circ - \phi) + T_{\perp} \cos(45^\circ - \phi)]$$

In these relationships,  $T_r$  is right circularly polarized radiation,  $T_l$  is left circularly polarized radiation,  $T_{\parallel}$  is linearly polarized radiation parallel to  $\mathbf{B}$  projected onto the plane of the sky, and  $T_{\perp}$  is linearly polarized radiation perpendicular to  $\mathbf{B}$  projected onto the sky. In all cases involving a spectral line, T, hence the Stoke parameters, are understood to be a function of frequency across the spectral line.

The total polarized Intensity is described by:

$$I(p) = (Q^2 + U^2 + V^2)^{1/2}.$$

Observations of linear polarization are stated in terms of the fractional polarization  $I_p/I$  and the position angle  $\Psi$  of the major axis of the polarization ellipse, where  $\Psi = (1/2) \arctan(U/Q)$ .

The Stokes parameters as defined in the above equations can then be expressed in terms of the Zeeman components for the normal Zeeman effect (see §4.1.2). In principle, the spectra of the Stokes parameters Q, U, and V for the Zeeman components provide full information about the magnetic field strength and direction. In practice Q and U signals are found to be extremely weak because they depend on the 2<sup>nd</sup> derivative of the I spectrum. However, the Zeeman effect is detectable in the stokes V spectrum which is dependent on the *first* derivative of the I spectrum (Crutcher et al. 1993). Observations making use of circular polarization measure the intensities of the right and left circularly

polarized components. The polarization techniques outlined above are described in detail below.

#### **4.1.1 Linear Polarization Techniques**

Linear Polarization techniques such as dust polarization, polarized grain emission, and synchrotron radiation emission are useful in determining magnetic field orientations. Davis and Greenstein (1951) first pointed out that rotating, non-spherical dust grains tend to align with their long axes perpendicular to the magnetic field. The dust grains will then preferentially absorb starlight with the E-vector parallel to the grains' long axes. Thus, light with vectors perpendicular to the interstellar magnetic field will tend to be blocked more than other light, leading to a net linear polarization parallel to the magnetic field. The polarization of starlight due to dust was first observed in 1949 by Hiltner and Hall, and has since been used to map the large-scale structure of magnetic field in the galaxy.

Thermal radiation emitted by the dust is also polarized due to dust grain alignment, giving rise to polarized grain emission. The magnetically aligned grains emit radiation preferentially along their long axes. Therefore, the net linear polarization is *perpendicular* to the magnetic field, not parallel to it as in the case of starlight polarization. This technique is useful in mapping the morphology of the magnetic field in dense molecular cloud cores using infrared and millimeter wavelength observations of linearly polarized dust grain emission. In such regions, optical extinction is so high that the polarized emission of background stars cannot be detected.

Synchrotron radiation is polarized perpendicular to the interstellar magnetic field and is due to the acceleration of relativistic electrons by a magnetic field. Because of the Lorentz Force, energetic electrons will spiral around the magnetic field lines. This motion causes the emission of strongly polarized continuous radiation or synchrotron radiation, where the intensity at a given frequency depends upon the field strength and the energy of electrons. Thus, the polarization of starlight should be perpendicular to the synchrotron emission, a fact which has been verified observationally.

### 4.1.2 Circular Polarization Techniques

For the purposes of the projects to be discussed in this document, the main method utilized in observation is the Zeeman Effect. The Zeeman effect arises from the interaction between an atom or molecule's net electronic magnetic moment and an external magnetic field. This effect results in the splitting of atomic or molecular energies levels with a frequency shift equal to

$$\Delta\nu = g\mu_B B/h$$

where  $g$  is the Lande  $g$  factor,  $B$  is the magnetic field strength, and  $\mu_B$  is the Bohr magneton for an electron. For species with a net nuclear magnetic moment, the Bohr magneton must be replaced with the nuclear magneton which is only about  $10^{-3}$  times as large owing to the much higher mass of the proton compared to the electron. It is the alignment or anti-alignment of the magnetic moment that results in the positive and negative frequency shifts.

The normal Zeeman effect arises when the magnetic splitting of the sublevels is the same in the upper and lower levels of the transition (or when the lower level is unsplit). This simple case can be envisioned with a classical model consisting of three oscillating charges. In the absence of an external magnetic field, all three oscillators are assumed to have the same frequency. One charge oscillates linearly along the direction of the external magnetic field. The other two charges oscillate in opposite directions in circles perpendicular to the field direction. Since no Lorentz force applies to the linear oscillator, its frequency is unaffected by the magnetic field. However, the circular oscillators are affected by the Lorentz force, so their frequencies are shifted by  $\Delta\nu$ . Since the Lorentz force acts in opposite directions for the two circular oscillators, one oscillator is shifted up in frequency by  $\Delta\nu$ , and the other is shifted down by the same amount. Therefore, the combined radiation of the three oscillators consists of three frequencies, the undisturbed frequency from the linear oscillator (known as the  $\pi$  component), and the  $\pm \Delta\nu$  frequencies from the circular oscillators (known as the  $\sigma$  components). Moreover, an observer looking perpendicular to the magnetic field direction will see the  $\pi$  component linearly polarized parallel to the field and the  $\sigma$  components linearly polarized perpendicular to the field. Conversely, an

observer looking along the magnetic field will not observe the  $\pi$  component at all and will see the  $\sigma$  components with opposite circular polarizations. Observed at an arbitrary angle to the magnetic field, the  $\pi$  component is linearly polarized along the field while the  $\sigma$  components have orthogonal elliptical polarizations with their major axes perpendicular to the magnetic field.

In cases where the normal Zeeman splitting much exceeds the observed line width (e.g. interstellar masers), observations of the total intensity  $I$  profile reveal three clearly separated line components, one  $\pi$  Zeeman component and two  $\sigma$  components. We refer to this case as the *strong field* case. In this situation, the total magnetic field strength can be directly inferred from measurement of the frequency shift between the two  $\sigma$  components. However, most astronomical situations, including all those described in this project, involve a frequency shift that is a tiny fraction of the line width (typically 1%). This is the *weak field* case. In such cases, more limited information about the magnetic field strength can be inferred from the Stokes parameter  $V$  profile. To understand this limitation, consider an observer looking along the magnetic field direction. Viewed from this angle, the two  $\sigma$  components are 100% circularly polarized and, of course, shifted by  $\pm \Delta\nu$ , where  $\Delta\nu$  is determined by the total field strength. Therefore, such an observer measures the full field strength, just as in the strong field case. Now imagine an observer looking at an arbitrary angle to the field in the weak field case. Although the frequency shifts  $\pm \Delta\nu$  are the same, the circular polarization in the spectral line is less because the radiation from the  $\sigma$  components is now elliptically polarized (i.e. less circularly polarized and more linearly polarized). So Stokes parameter  $V$  in the spectral line (the measured quantity) is weaker. In practice, the observed Stokes parameter  $V$  is proportional to the component of  $B$  along the line-of-sight. (See Crutcher et al. 1993 for a complete discussion.) Therefore, the weak field case does not reveal the total magnetic field strength, only that component (including its sign) along the line-of-sight.

As outlined above, detection of the Zeeman effect in the weak field case involves observation of Stokes parameter V. In practice, we observe  $T_r$  and  $T_l$  separately with the radio telescope system, obtaining a line profile for each sense of circular polarization. From these two profiles, we construct Stokes  $V = T_r - T_l$  and Stokes  $I = T_r + T_l$  (see above). For a small Zeeman splitting (weak field), the Stokes parameter V profile is the difference between two identical line shapes that are shifted slightly in frequency. Inevitably, this difference profile has the shape of the derivative of the total intensity Stokes I profile of the spectral line. Therefore, we can perform a least squares fit of the Stokes V profile to the derivative of the Stokes I profile using the equation of condition

$$V(u) = 1/2(ZB\cos\theta)(dI(u)/du),$$

where  $Z = g\mu_B/h$  and  $\theta$  is the angle between the magnetic field and the line of sight. Because there is no way to independently measure  $\theta$ , this method is sensitive only to the line-of-sight component of the magnetic field (i.e. to  $B\cos\theta$ ). For the purpose of the projects described below, the Zeeman effect will be utilized in observations of molecular cloud cores detecting 18cm OH and in measurements toward HII regions detecting 21cm HI. Both the 21 cm (1420 MHz) line and the two main lines of OH at 1665 and 1667 MHz are subject to the normal Zeeman effect as described above (Fig. 1.1).

## 4.2 Atomic and Molecular Zeeman Effects

The Zeeman effect as described above can be observed in both atomic and molecular species. Below are described the atomic and molecular transitions that give rise to the Zeeman effect in 21 cm Hydrogen and 18 cm Hydroxyl (OH).

### 4.2.1 Atomic Hydrogen (HI)

The ground ( $n=1$ ) state of the neutral hydrogen atom has two hyperfine levels separated by a very small energy difference. This phenomenon occurs due to the spin of the electron and the proton which generates a magnetic dipole moment. Two possible ground states of the hydrogen atom can exist: the state where the dipole moment vectors of the proton and electron are parallel and the



state where these vectors are antiparallel. The aligned state will be at a slightly higher energy than the opposed state, giving rise to the hyperfine splitting.

The hyperfine splitting of the ground state of the hydrogen atom can be described quantum mechanically in the following manner; the ground state configuration of the hydrogen atom is  $^2S_{1/2}$ , where the orbital angular momentum  $L=0$  and the electron spin angular momentum  $S=1/2$ . The nuclear or proton spin,  $I=1/2$ . We can define the total angular momentum of the system,  $F$  as,

$$\mathbf{F}=\mathbf{J}+\mathbf{I}$$

where  $\mathbf{J}=\mathbf{L}+\mathbf{S}$  and describes the total angular momentum without nuclear interactions.

Hyperfine interactions with the nuclear spin splits the ground state into 2 hyperfine levels  $F=J+I=1$  and  $F=J-I=0$ . In the presence of a magnetic field each  $F$  state further splits into  $2F+1$  magnetic sublevels. The wavelength of the transition between the  $F=1$  and  $F=0$  states is 21 cm with a corresponding frequency of 1420 MHz . Figure 1.2 shows the level diagram for the ground state of atomic hydrogen in the presence of a magnetic field.

#### 4.2.2 Hydroxyl (OH)

Zeeman effects in molecules are comparable to the HI Zeeman effect only in molecules having electronic angular momentum (either orbital or spin). In such cases the Zeeman effect is related to the Bohr rather than the nuclear magneton (see §4.1.2 above). Only molecules with an odd number of electrons in their outer shell have net angular momentum. One example is OH, the hydroxyl radical, which has an unfilled electron shell and various internal spins. As for all diatomic molecules, the electric field of the nuclei of OH molecule is symmetric around its inter-nuclei axis. Therefore, there are no torques upon the electrons about this axis, and  $L_z$  is conserved. We define  $L_z \equiv \Lambda$ ,  $S_z \equiv \Sigma = \pm 1/2$  and  $J_z \equiv \Lambda \pm \Sigma = \Lambda \pm 1/2$ . The total angular momentum, excluding nuclear spin is described by,

$$\mathbf{J}=\mathbf{K}+\mathbf{L}+\mathbf{S}$$

where  $\mathbf{K}$  is the molecular end-over-end rotation,  $\mathbf{L}$  is the electronic orbital angular momentum and  $\mathbf{S}$  is the electron spin (Elitzur 1992).

The ground electronic state is  $\Lambda=1$  or a  $\Pi$  state where  $\Sigma$ ,  $\Pi$ ,  $\Delta$ , denote  $J_z=0,1,2$ . Thus  $J_z=1\pm 1/2$  which gives rise to two rotation ladders  ${}^2\Pi_{1/2}$  and  ${}^2\Pi_{3/2}$ , where the superscript 2 corresponds to the two possible electronic spin orientations and the subscript 3/2 corresponds to  $J_z$  (Elitzur 1992). The lowest lying  ${}^2\Pi_{3/2}$  state is a lambda doublet with a separation of the doublet corresponding to a frequency of about 1666 MHz. A lambda doublet is produced by the interaction between the electronic orbital angular momentum and the angular momentum of molecular rotation. For a diatomic molecule, there are usually two degenerate states associated with the orientation with respect to the inter-nuclear axis of a non-zero value of  $\Lambda$  ( $+\Lambda$ ,  $-\Lambda$ ). However, if one of the atoms in the diatomic molecule is more massive than the other (as in OH where oxygen is  $\sim 16$  times more massive than hydrogen), these orientations are not exactly equivalent, and the two states ( $+\Lambda$ ,  $-\Lambda$ ) have slightly different energies.

Further splitting of each level of the lambda doublet is due to the hyperfine interaction with the nuclear spin  $I=\pm 1/2$ . The total angular momentum is thus,

$$\mathbf{F}=\mathbf{J}+\mathbf{I}$$

where  $\mathbf{F}$  is the total angular momentum including nuclear spin. Hyperfine interactions between the electrons and proton, split each lambda-doublet state into two levels corresponding to  $F=2$  and  $F=1$ .

The allowed transitions for OH are governed by selection rules with the wavelength of the ground state transitions being approximately 18cm. The  $F=1\rightarrow 1$  and  $F=2\rightarrow 2$  transitions have frequencies of 1665 MHz and 1667 MHz respectively and are called main lines. The  $F=1\rightarrow 2$  and  $F=2\rightarrow 1$  transitions have frequencies of 1612 and 1720 MHz respectively and are called satellite lines. In the presence of a magnetic field each hyperfine level is split into  $2F+1$  magnetic sublevels. The two main lines each come from an upper and lower state having the same value of  $F$ , meaning the Lande  $g$  factors, or magnetic splitting factors, for the upper and lower states of each transition are the same (Fig. 1.3). This gives rise to the normal Zeeman effect as described in §4.1.2.

## **5. Project Description**

The object of this dissertation is to provide an observational study of the effects of interstellar magnetic fields on star-formation regions. This is part of a long-standing research project that uses the techniques of radio astronomy to measure magnetic field strengths in the interstellar medium of our galaxy. Interstellar magnetic fields are believed to play a crucial role in the star-formation process therefore a comprehensive study of magnetic fields is necessary in understanding the origins of stars (and planets, by implication).

### **5.1 NGC 6334 A**

Our efforts in this project have been focused on NGC 6334 A, a compact HII region at the center of what is believed to be a large, rotating molecular torus (based on studies by Kramer et al. 1997). This is a continuing study based on initial measurements of the HI and OH Zeeman effect (Sarma et al. 2000). The current study includes OH observations performed by the Very Large Array (VLA) at a higher spatial resolution than previously published data and allows for a better analysis of the spatial variations of the magnetic field. We have also extended this study to include a complete analysis of the environment of NGC 6334 A including the associated atomic and molecular gas.

### **5.2 Cygnus X**

For this project, magnetic fields in the “Cygnus-X” region of the Galaxy have been studied. This region lies along the galactic plane centered at a longitude of approximately  $80^\circ$ . The line-of-sight through this region lies along a spiral arm of the Galaxy. This region is geometrically favorable for Zeeman effect observations, due to the sensitivity of the Zeeman effect to the line-of-sight magnetic field. Also, galactic magnetic fields are known to be oriented, in general, along spiral arms. The observations to be described are intended to measure magnetic field strengths in these regions in order to make a determination of the mass-to-flux ratio, and thus determine the role of the interstellar magnetic field in the dynamics and evolution of the region.

The VLA has been used in this project to study the Zeeman effect in the 21cm HI line seen in absorption against radio sources in the Cygnus-X region.

These sources are mostly galactic nebulae or HII regions, and are bright and compact in this region of the spectrum. Therefore, HI absorption lines are strong against these regions and the VLA is capable of detecting the weak Zeeman effect within them.

$$V(\nu) = \left( \frac{ZB \cos \theta}{2} \right) \frac{dI(\nu)}{d\nu}$$

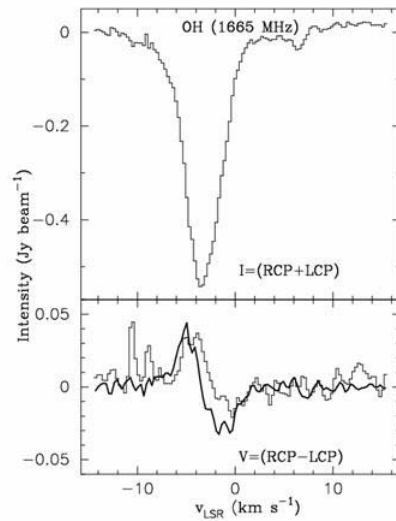


Fig. 1.1 -Estimating the Magnetic Field Strength; Stokes I (*Top*) and V (*Bottom*) profiles in the OH 1665 MHz Line toward NGC 6334 Source A at the position  $\alpha=17^{\text{h}}16^{\text{m}}58^{\text{s}}.5$ ,  $\delta=-35^{\circ}51'35''$ . The continuous line superimposed on the V spectrum in the lower box is the derivative of I scaled by the derived value of  $B_{\text{los}}=595\pm 101\mu\text{G}$

### Normal Zeeman Effect Splitting

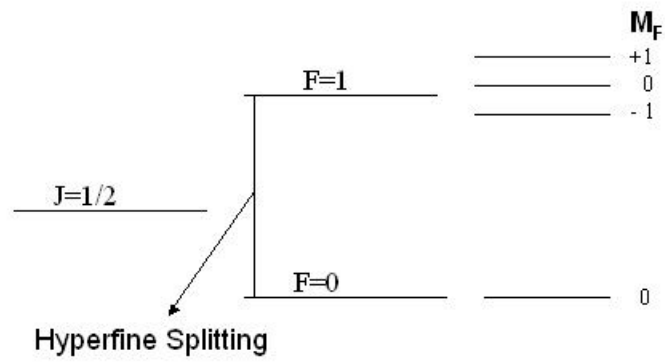


Fig. 1.2 –Ground state of HI in the presence of a magnetic field.

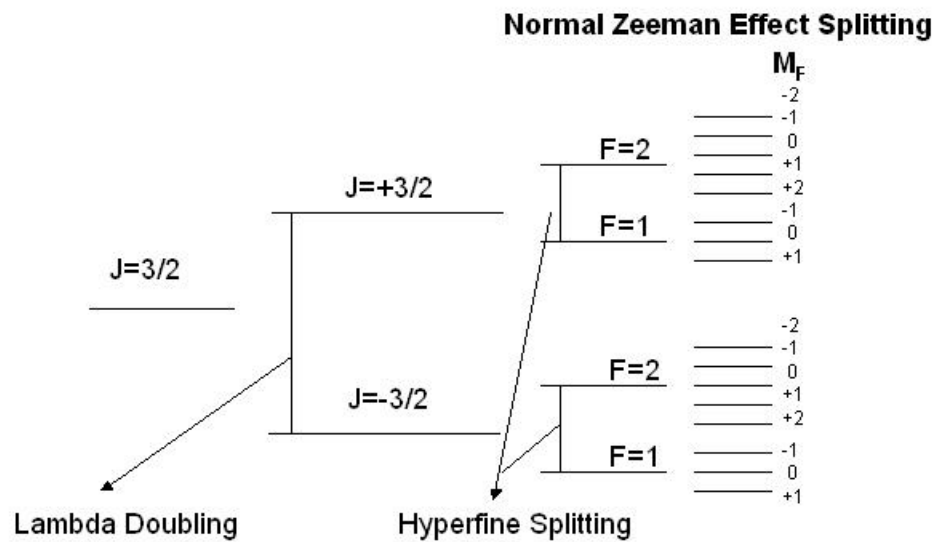


Fig. 1.3 -Ground state of OH in the presence of a magnetic field.

## Chapter 2. VLA Data Reduction Calibration and Editing Procedures

### 1. Introduction

A good deal of time and effort was put into the data reduction process for the VLA observations described in this thesis. Therefore, I have provided below an overview of the calibration and editing applied to our observations before any analysis could take place. As standard calibration techniques are well documented, the focus of this section is the removal of masers from a field in which Zeeman measurements are to be made. I have included a detailed description of the self-calibration and maser subtraction procedure that was applied to the NGC 6334 observations due to contaminating OH masers in the field of view.

Many of the operations described below were performed using the Astronomical Image Processing Software (AIPS), a standard data reduction package for VLA data. The data calibration and editing processes described assume a familiarity with synthesis imaging techniques.

#### 1.1 Radio Interferometry

The angular resolution of a telescope depends on the wavelength of the observations divided by the aperture of the instrument:

$$\theta = \lambda/D$$

where  $\theta$  is the angular resolution of the telescope in radians,  $\lambda$  is the wavelength of the observations, and  $D$  is the aperture of the instrument. Radio telescopes operate at much longer wavelengths compared to optical telescopes and therefore must be much larger to achieve the same angular resolution. A large single antenna when used at its shortest operating wavelength typically achieves a resolution little better than 1 arc minute, comparable to the unaided human eye at optical wavelengths. For example, a single dish radio telescope with an aperture of 100m, observing at a wavelength of 21cm (the wavelength for which the Zeeman effect in neutral hydrogen is observed) has an angular resolution of 7 arc minutes. In order to achieve higher angular resolution, it is possible to synthesize a very large effective aperture from a number of smaller elements.



This is the principle behind radio interferometry, for which, subject to some important limitations, the relevant value of  $D$  is the distance between two radio telescopes, not the diameter of each.

As an example, consider a simple two-element radio interferometer. A signal received from a point-like or unresolved source will arrive at each element alternately in phase and out of phase as the Earth rotates, owing to changes in the path difference from the radio source to the two elements. Therefore, the sum or the product of the output from the two elements varies sinusoidally, creating interference “fringes”. These fringes are similar to those produced at optical wavelengths by, for example, the two slit experiment. If the radio source has a finite angular size (an extended source), the path length difference to the elements of the interferometer varies across the source. In such a case, the amplitude of the sinusoidal fringes may be lessened. Thus, the interference fringe amplitudes measured at an interferometer pair depend on the details of the distribution of emission from the radio source or what is known as the “brightness distribution.” The fringes also depend upon the separation of the two radio telescope elements in wavelength units, where the separation is measured in a plane perpendicular to the line-of-sight to the source (i.e. the *projected* separation). Moreover, this projected separation changes as the Earth rotates.

The interference fringes measured at the interferometer pair is one Fourier component of the two-dimensional brightness distribution of the source. These components are complex visibilities described by,

$$V_{ij,t} = Ve^{i\phi},$$

where  $V$  is the amplitude and  $\phi$  is the phase of the fringe pattern. Both are slow functions of time as the Earth rotates. The phase  $\phi$  is relative to the phase of a hypothetical pattern created by a point source at the center of the field of view of the two radio telescope elements. Several interferometer pairs, combined with Earth rotation, can sample large numbers of Fourier components from which high resolution images can be reconstructed through Fourier transform, thus synthesizing the effect of a large single aperture. For example,  $n$  antenna elements create  $n(n-1)/2$  interferometer pairs. For the Very Large Array (VLA,

see below)  $n = 27$  if all antennas are operating. So the array simultaneously measures fringe visibilities for 351 antenna pairs (<http://www.vla.nrao.edu/>).

## 1.2 The Very Large Array (VLA)

The VLA is a 27 element interferometric array which is able to produce images at a wide range of frequencies and resolutions. Each of the 27 radio telescopes is moveable such that the array can vary its resolution over a range exceeding a factor  $\sim 50$ . The four basic arrangements or configurations are denoted as D, C, B, and A whose scales vary by the ratios 1 : 3.2 : 10 : 32 from smallest to largest. There are also 3 hybrid configurations denoted as DnC, CnB, and BnA, in which the antennas in the northern arm are deployed in the next larger configuration than the SE and SW arm. These configurations are used for observations of sources that are located south of declination  $= -15^\circ$  or north of declination  $= +75^\circ$ . By lengthening the northern arm, the projected distances between the array elements (i.e. baselines) of the array elements will approximately match those of the standard configuration for sources in the southern sky.

Each of the VLA antennas is permanently outfitted with receivers for seven frequency bands referred to as P, L, C, X, U, K, Q bands. In fact, there are two receivers installed on each antenna for each frequency band. These two receivers are completely independent, and they are sensitive to orthogonal senses of polarization. Our observations were performed at "L-band", centered at approximately 20 cm. This band is appropriate for observation of 21 cm hydrogen and 18 cm hydroxyl (VLA Status Summary). The VLA L-band system has receivers sensitive to orthogonal circular polarizations, so the difference between the responses of these two receivers is Stokes parameter V.

Signals for each of the VLA antennas are digitized and then multiplied together for each antenna pair (351 pairs at most) by a digital correlator. Moreover, the correlator can provide separate visibilities as a function of frequency within a defined bandpass. For example, for a bandwidth of 0.195 MHz there are 256 frequency channels available with a frequency separation of 0.763 kHz. Therefore, the ultimate product of a VLA observation (after Fourier transformation) is a series of images of the brightness distribution of the source,

with each image as a slightly different center frequency. Each center frequency is often described as a “channel”. Such a data set, characterized by two angular coordinates in the sky and a frequency coordinate or channel number, is often referred to as a “data cube”.

### **1.3 Observations**

The response of the VLA system is not identical for a series of adjacent frequency channels within a given bandpass. Instead, the response is low at the very lowest frequency channels and at the very highest ones, and the response reaches a broad peak over intermediate channels. The VLA response function with frequency over a given bandpass is called the “bandpass function”. In practice the bandpass function depends upon the receiver in use (two receivers sensitive to orthogonal polarizations), the bandpass selected (i.e. the total range in frequency spanned by the channels) and the particular pair of antennas for which visibilities are observed. Also, the bandpass function for any pair of antennas varies slowly with time.

Zeeman observations are sensitive to small variations in the bandpass function. The reason is clear since the Zeeman effect is derived from the difference in response between two receivers sensitive to opposite circular polarizations (i.e. Stokes V). In general, two receivers (with their different electronics and signal paths) will have somewhat different bandpass functions. So the difference in their responses will reflect these instrumental considerations as well as the true Stokes V. To mitigate this instrumental effect, we employ a front-end transfer switch on each telescope. These switches are reversed every 10 minutes during an observation, creating separate data sets identified as “qualifier 1” and “qualifier 2”. For data sets in the former category, the signals from each receiver are directed along their normal paths from the telescopes to the digital correlator. For data sets in the latter category, the signals from each receiver are directed along the paths normally used for the other receiver. With this technique, we can construct Stokes parameter V profiles independently for each receiver and then combine them into average Stokes parameter V profiles. This combination process effectively cancels out differences in the bandpass

functions for the two oppositely polarized receivers. This observing technique is described by Brogan and Troland (2001).

## 2. An Overview of Calibration and Editing of VLA Data

### 2.1 Standard Data Calibration

Standard data calibration is first applied in order to transform empirically, observed visibility amplitudes and phases into true amplitudes and phases. This process is analogous, in part to focusing a camera for the sharpest possible image. Calibration relies on the frequent observations of radio sources of known structure, strength, and position. We can describe the relationship between the observed and true visibilities as

$$\mathbf{V}_{\text{true } i,j,t} = \mathbf{V}_{\text{obs}} \mathbf{A}_{i,j,t}$$

where  $\mathbf{A}_{i,j,t}$  represents the effect of complex gains on the antenna elements and can be approximated by

$$\mathbf{A}_{i,j,t} = A_i(t)e^{i\phi_i(t)} A_j(t)e^{i\phi_j(t)}$$

where  $A_i$  and  $A_j$  are the single antenna-based amplitude and  $\phi_i$  and  $\phi_j$  is the antenna-based phase. Indices  $i$  and  $j$  refer to the two antennas making up a given interferometric pair at time  $t$ . Strictly speaking, the complex gain  $\mathbf{A}_{i,j,t}$  applies to a given pair of antennas since all interferometric observations are made with *antenna pairs*, not individual antennas. However, the approximation is usually made that  $\mathbf{A}_{i,j,t}$  is the product of the complex “gains” of individual antennas, as illustrated in the equation above. This approximation defines what is called “antenna-based” calibration, the alternative is “baseline-based” calibration for each antenna pair. The antenna-based approximation is very useful for large arrays such as the VLA that have a much larger number of simultaneous antenna pairs (351) than of antennas (27). For such arrays, the number of complex gains that must be determined in antenna-based calibration is dramatically smaller than for baseline-based calibration. Since fewer parameters are determined by the calibration visibility data sets, these parameters are much more accurately determined.

In practice, standard calibration is performed by observations of a calibration source, that is, a source with known flux density and well-determined

position on the sky. The calibration source must also be a point source that is unresolved by any antenna pair in the array. Since the flux and position of the calibration source is known in advance, all *calibrated* visibilities for such a source should have phases of zero and amplitudes equal to the flux density of the source. Therefore, the calibration procedure involves finding by least-squares solution those antenna-based gain factors  $\mathbf{A}_{ij,t}$  that, when applied to the uncalibrated visibilities, correct them to the known values for the calibration source itself. This least-squares solution is very overconstrained because there are so many more antenna *pairs* than antennas in the VLA. Once the gain factors are determined for the calibration source, they may then be applied to the program source for which the visibilities are not known *a priori*. Since the calibration source is observed periodically (typically at least once per 30 minutes), the antenna gain factors can be solved for and later applied to the program source data as a function of time.

In standard calibration of VLA data, there is a model of the source from which all the expected phases and amplitudes of all source visibilities can be computed. We use the AIPS task CALIB to model the phase calibrator(s) as a point source(s) at the phase center such that all visibility phases are expected to be zero and all visibility amplitudes are expected to be equal the flux of the calibrator source(s), where the flux density scale has been set by the AIPS task GETJY.

CALIB performs a least-squares fit involving visibilities from all available baselines. This fit is possible because CALIB has access to all of the uncalibrated complex visibilities from the uv data base and also CALIB knows the “true” complex visibilities from the source model. From this input information, CALIB can determine the values of the antenna-based phase offsets and the antenna-based amplitude gain factors. The solutions determined by CALIB are stored in the solution (SN) table written into the input uv or visibility data set.

We use the AIPS task CLCAL to build the final calibration table (CL) which will be applied to the data set. CLCAL will fill the CL table with the antenna gains and phase solutions determined from CALIB for each phase calibrator. CLCAL is

also used to determine these parameters for the program source itself based on the phase calibrator solutions and a 2 point interpolation function. The final CL table is applied to program source continuum and spectral line data.

## **2.2 Data Flagging**

The goal of a flagging procedure is to eliminate obviously discrepant uv data points, typically these are amplitudes that are much higher than expected. The flagging procedure is applied originally to uncalibrated uv data. The initial flagging begins with the CH0 data set. The CH0 data is created by averaging in frequency the channels of the central 75% of the band. Flagging of the line data set is only considered after the flagging and calibration of the CH0 data set. Also, to begin with only calibrator data are flagged prior to the calibration unless there are obvious bad data in the program source data.

I have found it useful to plot uv visibility amplitudes vs baseline using the AIPS task UVPLT to determine if there are any obvious bad amplitudes and what range of amplitudes need to be flagged. There are several editing tasks which can be used to flag data, I prefer to use TVFLG. TVFLG is an interactive editing task in AIPS which displays plots of amplitudes or other parameters (such as phases) as a function of baseline or time. It has several options for flagging such as single point flagging to flagging data over a range. It also allows simultaneously flagging of right and left circularly polarized data.

## **2.3 Self-Calibration and Maser Subtraction**

OH masers in the field of view can effect Zeeman analysis of the data because masers are often highly polarized. Moreover, maser effects can spread over the entire field of view in dirty maps owing to sidelobes of the synthesized beam. There are two strong masers in the field of view of NGC 6334 and several weaker masers. The strongest maser (~400 Jy) coincides with source F, the next strongest (~50 Jy) lies within the shell-like region to the southwest of source A. Both masers are well separated from NGC 6334 A. Fluxes given are the sum of right and left polarization at 1665 MHz, Stokes parameter I. Maser radiation is confined to the LSR velocity range -5 km/s to -14 km/s. This range includes the low velocity wing of the principal OH absorption line component.

We attempted to mitigate OH maser effects in the data set using an iterative process in AIPS. This process, similar to that employed by Sarma et al (2000), relies upon careful self-calibration of the data. In very well calibrated VLA data, the images are “sharp” in the sense that the actual point source response is very similar to the theoretical point source response, the “dirty beam”. In such a case, it is possible to subtract out maser effects in the uv plane by modeling the masers as sums of point sources (i.e. dirty beams). To accomplish this task, we first chose the frequency plane in a uv data cube with the strongest emission from the 400 Jy maser. (This calibration plane was different for each OH line and each circular polarization owing to high circular polarization of the masers and their different velocity structures in the different lines). Then we subtracted the continuum flux from this calibration plane with AIPS task UVLSF, leaving only maser emission in the uv data. Next we performed several iterations of self-calibration. For each iteration we imaged the plane with IMAGR and identified clean components in a small circular zone centered on each of the two strong masers. These clean components served as the source model for self-calibration of the plane with CALIB. Next we applied the self-calibration solution to the uv data for this plane, re-imaged the plane, and identified clean components once again for the masers. When further iterations yielded little change in the maser clean components, we judged that the best possible self-calibration had been achieved for the calibration plane. In total, we performed three iterations of self-calibration solving for antenna-based phases only and a final iteration solving for antenna-based phases and amplitudes.

To remove maser effects in the entire uv data cube, we first applied the final self-calibration solutions to all frequency planes of the cube. Next we re-imaged each frequency plane having maser emission (planes in the velocity range -5.2 to -14.5 km/s), we identified clean components associated with the two strong masers in each plane, and we used UVSUB to subtract out the contributions of these clean components to the uv data. Finally, we re-imaged the resulting uv data cube to create maser-free images for each frequency channel. Of course, this entire self-calibration and maser subtraction process

was performed independently for each OH line (1665 and 1667 MHz), each day of data and each circular polarization. Once the process had been applied to all data, we constructed maser-free Stokes I and V data cubes for each OH line.

With this maser subtraction process, we reduced maser contamination very significantly in pixels of Zeeman interest toward NGC 6334 A. However, this suppression was insufficient to permit reliable use of these channels for Zeeman analysis of the thermally-excited OH absorption lines. Therefore, the Zeeman analysis described in chapter 3 excludes most of these channels. A more detailed, step-by-step procedure for the self-calibration and maser subtraction process outlined above is described in §3.

### **3. Self-calibration and Maser Subtraction Procedures for NGC 6334**

The procedure below should be applied for maser contaminated fields after the standard VLA calibration has been applied.

#### **3.1 Preliminary Data Preparation**

- Using BPASS, bandpass calibrate the data using the primary flux calibrators as the calibration sources.
- Using SPLIT, apply the standard calibration (CL), flag (FG), and bandpass (BP) tables to the data.
- Using SPLIT, apply Hanning Smoothing [Smooth(1)=1] to eliminate ringing due to masers.
- Using SPLIT, separate polarizations into LL or RR (STOKES=LL or RR).
- Create preliminary data cube using IMAGR and transform into FITS file using FITTP. Determine channel to use for self-cal.
- Using UVLSF, subtract continuum, setting order parameter appropriately. The proper channels for subtraction can be determined in Aipsview.

#### **3.2 Self-calibration**

- Using SPLIT separate channel for self-calibration. The channel should have strong maser flux, and if more than one maser, both should be used in self-calibration for best model.



- Using emacs or another editing program, create a Boxfile for clean component boxes. Set field centers in this file.
- Set boxes interactively for clean component model in IMAGR, specifying the same name for BOXFILE and OBOXFILE such that IMAGR will overwrite any changes made to file.
- Run IMAGR on the original SPLIT file (the file with the separated channel), setting FLUX to  $-1$  such that it stops at the first negative clean component. Set NITER to something such as 20000. Set OVERLAP to 1 such that it cleans each window iteratively. We have been setting the gain loop to .1 (GAIN) and MINPATCH to  $-121$ . We want a small IMSIZE (for NGC 6334 we used 128x128) to save disk space and the CELLSIZE should oversample the beam (there should be a few pixels across the beam.)
- Look at clean component table with task PRTCC, look at the amount of flux in each clean component for comparison with later CC tables.
- Run CALIB on the original SPLIT file, using the CC table in the previously made image file as the model. Set SOLMODE to P (phase) and SOLINT to 1 or 2 minutes depending on the number of closure errors. For NGC 6334 the masers are strong enough such that there are no closure errors and the SOLINT can be set to 1 min. The output will be an SN table in the original SPLIT file and a .Calib file.
- Run IMAGR on the .calib file to create a new CC table. Keep parameters as above.
- Look at CC table and compare with the earlier version.
- Run CALIB on the original SPLIT file using the CC created by the previous IMAGR run for the model. Keep SOLINT and SOLMODE as above. This will create SN table 2 in the original SPLIT file and a new .calib file.
- Run IMAGR on the new .calib file to create a new CC table. Keep parameters as above.
- Look at CC table and compare with earlier versions, if there is significant differences repeat above steps. If there is very little difference, proceed below.

- Run CALIB on the last .calib file created by the last CALIB run. Use the CC table created by the previous IMAGR run for model. Set SOLINT to 10 min. and SOLMODE to A&P (amplitude and phase). This will create SN version 1 in the .calib file and a new .calib file.
- Image final .calib file, and then check RMS noise for each file.
- Note: It is a good idea to examine the SN tables using SNPLT between runs of CALIB to look for unusual trends, etc.
- Using TACOP copy the highest version of the SN table from the original SPLIT file to both the continuum subtracted and non-continuum subtracted data cube. Use SPLIT to apply the table to the cubes and create a new calibrated data cube. Using TACOP on the new calibrated data cubes, copy the SN table from the .calib file. Use SPLIT to create final calibrated data cubes to be used in maser subtraction.

### 3.3 Maser Subtraction

- Using MOVE make copies of both calibrated uv data cubes, because UVSUB will overwrite original data cubes.
- Using IMAGR make a cleaned image cube from the continuum subtracted uv data cube, setting FLUX to -1 to stop at first negative clean component. We want to use the same Boxfile and keep the IMSIZE small (for example 128x128) to save disk space.
- Using UVSUB, subtract out the channels in which the maser is evident. It is very important for the INFILE, INSEQ, and INCLASS to be EXACTLY the same as the OUTFILE, OUTSEQ, and OUTCLASS. In other words the INFILE will be overwritten. The INFILE specified should be the non-continuum subtracted data cube, and the CC table from the previous IMAGR run should be used for the model. Set CHANNEL to 0 and INVERS to 0 and use the following commands to run UVSUB on ONLY the maser channels: For example if you want to run UVSUB on channels 80-120 enter, **for i=80:120; channel=i; invers=i; go uvsub; wait uvsub; end.** OPCODE should be set to " to subtract model visibilities from observed and CMETHOD to dft for direct fourier transform.

- Make a dirty image cube of maser subtracted data using IMAGR to check how well the maser's subtracted out. Increase IMSIZE for a full field of view.

### 3.4 Creating Stokes I and V Cubes

- Using DBCON combine data cubes containing all qualifier information, information from different days, and matching polarizations for each frequency. This will create 2 data cubes containing RR and LL polarizations respectively.
- Image each of the RR and LL data cubes. Box continuum sources interactively in IMAGR. Clean to an appropriate flux level, usually some multiple of the rms noise. Alternatively, to determine flux level, you can image a line free plane with FLUX set very low and NITER high, and watch the imaging run looking for the point where IMAGR begins cleaning at the noise level.
- Create a FITS file of the image cube, and examine to determine channels for continuum subtraction.
- As above, use UVLSF to create continuum subtracted data cubes.
- Use COMB to create I and V cubes. Working in the image plane select the RR and LL image cubes as the inname and in2name, and create I and V by choosing OPCODE 'sum' and setting the APARMS as necessary; for example APARAM 1, -1,0 will subtract LL from RR. For NGC 6334, we used non-continuum subtracted I cubes for the Miriad procedures to determine  $B_{LOS}$ .

### 3.5 An Index of AIPS Tasks

I have provided below an index of the AIPS tasks used in the above procedures. AIPS is arranged such that the tasks perform the main operations on the data and what are known as verbs and adverbs are the parameters inside each task. Below I describe the function of each task used in the self-calibration and maser subtraction. This information is provided from the AIPS help manual and AIPS Cookbook.

<b>BPASS</b>	Task to create a 'BP' (bandpass) table which will contain the bandpass response functions of the antennas.
<b>CALIB</b>	This task determines the calibration to be applied to a uv data set given a model of the source(s).
<b>COMB</b>	COMB is a generalized task which combines two input images and, optionally two input noise images, pixel by pixel to produce a new cataloged image and, optionally, an image of the uncertainty in the main output image.
<b>DBCON</b>	Task to concatenate two uv databases.
<b>FITTP</b>	FITTP converts the standard header and map or uv data and writes it on a output tape in the FITS format.
<b>IMAGR</b>	A Wide field imaging/Cleaning task.
<b>PRTCC</b>	PRTCC prints on the line printer or terminal the rows of extension files containing clean components in the tables format.
<b>TACOP</b>	TACOP copies AIPS extension files, principally those of table type.
<b>UVLSF</b>	This task does a spectral baseline subtraction.
<b>UVSUB</b>	Subtracts/divides a model from/into a uv data base.

# Chapter 3. VLA OH Zeeman Observations and Complete Environmental Analysis of NGC 6334 A

## 1. Introduction

### 1.1 The Zeeman Effect and Magnetic Fields

The Zeeman effect in radio frequency spectral lines provides a measure of magnetic field strengths of molecular clouds. From this information, one can evaluate the importance of magnetic fields to the dynamics and evolution of these star-forming regions. For non-maser lines, the Zeeman splitting is a small fraction of the line width, so it is only sensitive to the line-of-sight component of the magnetic field,  $B_{\text{los}}$  (Crutcher et al 1993).

In this chapter we discuss high spatial resolution Zeeman effect observations of 1665 and 1667 MHz OH absorption lines toward radio continuum source A of the NGC 6334 complex (NGC 6334 A). We also consider the environment of NGC 6334 A including its associated atomic and molecular gas. This study represents a significant extension of the work of Sarma et al. (2000). In the remainder of §1 we review some details of the NCG 6334 complex with a focus on radio continuum source NGC 6334 A; §2 details the observations and reduction of the data; §3 presents the results of our observations, §4 contains discussion of these results, and §5 conclusions drawn from our observations.

### 1.2 The NGC 6334 Complex

NGC 6334 is a giant molecular cloud (GMC) complex and star forming region at a distance of 1.7 Kpc (Neckel 1978). It lies about 0.5 degrees above the galactic plane and extends  $\sim 30'$  (15 pc) parallel to it. Radio continuum emission from this region was mapped at 6 cm with the VLA by Rodriguez, Canto & Moran (1982, hereafter, RCM82). They found six discrete continuum sources lying along a ridge of radio emission parallel to the galactic plane. RCM82 labeled these sources A through F, a nomenclature we adopt in this paper (see Fig. 3.1). Subsequent studies of the NGC 6334 region have been performed at various wavelengths, and an overview of these studies can be found in Sarma et al. 2000. Further discussion of the NGC 6334 region appears in Munoz et al. (2007).

### 1.2.1 Source A

NGC 6334 A, also known as NGC 6334 IV, is an ultra-compact HII region (UCHII) with a shell-like morphology. Its structure was first described by Rodriguez, Canto & Moran (1988, hereafter, RCM88) on the basis of 6 cm radio continuum emission. The 6cm continuum emission studies of RCM88 showed that extending from a central shell are two fainter lobes of ionized gas. These features are usually referred to as the northern and southern lobes. Higher resolution radio continuum studies by Carral et al. (2002) show the central shell to contain irregular clumps, with a significant break in the clumps in the direction of the southern lobe. This study shows the shell to have a diameter of  $\sim 15''$  (0.12 pc) and a thickness of  $\sim 2''$  (0.016 pc). Carral et al. also discovered an unresolved, compact radio source at the center of the central shell. They suggest this source is associated with the ionizing star or stars for the shell, with the radio emission arising from ionized stellar winds. Their favored model to explain the shell-like morphology of NGC 6334 A is a wind-driven bubble in which mechanical input from the stellar wind dominates the dynamics and evolution of the region.

The northern and southern radio continuum lobes have been described as arising from a flattened cloud of neutral gas that confines the HII region in an east-west direction but allows radiation and matter to escape to the north and south (RCM88). In this sense, NGC 6334 A is pictured as a biconical or bipolar HII region, similar to S106 (Roberts et al. 1995). Observations of millimeter wavelength molecular emission lines by Kraemer et al. (1997) identified a flattened molecular cloud centered on NGC 6334 A. The dimensions of this cloud are  $2.2 \times 0.9$  pc, elongated in the east-west direction. From CO studies, they find an east-west velocity gradient of  $2.4 \text{ km s}^{-1} \text{ pc}^{-1}$ . They suggest that the flattened cloud is a rotating molecular torus with NGC 6334 A at its center. If so, the implied virial mass of the molecular torus is  $2400 \pm 1100 M_{\text{sun}}$ . In the discussion below, we refer to this structure as the molecular torus, although its geometry and state of rotation are not fully understood.

## **2. Observations and Data Reduction**

### **2.1 Observations**

Observations were carried out by the VLA in the BnA (1999) and CnB (1996) configurations. Array parameters are detailed in table 3.1. Both circular polarizations of the OH mainlines (1665 MHz and 1667 MHz) were observed simultaneously. A front-end transfer switch on each telescope was used to reverse the sense of circular polarization received at the telescope every 10 minutes in order to mitigate instrumental effects. This observing technique is described by Sarma et al. (2000).

### **2.2 Data Reduction**

Editing, calibration, Fourier transformation, deconvolution, and processing of the OH data were carried out using the Astronomical Image Processing System (AIPS). We combined data from BnA and CnB configurations using AIPS task DBCON to create a hybrid data set. Further data processing, including magnetic field calculations, were carried out in the Multichannel Image Reconstruction, Image Analysis and Display (MIRIAD) system (Sault, Teuben, & Wright 1995).

#### **2.2.1 An Attempt to Remove Maser Contamination**

OH masers in the field of view can affect Zeeman analysis of the data because masers are often highly circularly polarized. Moreover, maser effects can spread over the entire field of view in dirty maps owing to sidelobes of the synthesized beam. There are two strong masers in the field of view of NGC 6334 and several weaker masers. The strongest maser ( $\sim 400$  Jy) coincides with source F, the next strongest ( $\sim 50$  Jy) lies within the shell-like region to the southwest of source A. Both masers are well separated from NGC 6334 A in the field of view. There is also a weak (1 Jy) maser at 1665 MHz on the western edge of source A. Fluxes given are the sum of right and left polarizations at 1665 MHz, Stokes parameter I. Maser radiation is confined to the LSR velocity range - 5 km/s to -14 km/s. This range includes the low velocity wing of the principal OH absorption line component.

We attempted to mitigate OH maser effects in the data set using an iterative process in AIPS. This process, similar to that employed by Sarma et al (2000), relies upon careful self-calibration of the data. We provide details of the process in Chapter 2. With the maser subtraction process, we reduced maser contamination very significantly in pixels of Zeeman interest toward NGC 6334 A. However, this suppression was insufficient to permit reliable use of these channels for Zeeman analysis of the thermally-excited OH absorption lines. Therefore, the Zeeman analysis described in § 3.2.2 excludes most of these channels.

### **3. Results**

#### **3.1 Continuum Emission**

Figure 3.1 shows the 18 cm (1667 MHz) image of the continuum sources in the NGC 6334 complex. The 18 cm map was made by the AIPS task IMAGR at a resolution of 8.2"x 5.0" with a robustness of 1.5 (where a robustness of 5 is natural weighting). Individual radio continuum sources lie in a ridge that extends northeast to southwest and are labeled A through F, as described above, using the nomenclature of RCM82. (See, also, Sarma et al. 2000.) RCM82 concluded that all sources except B are HII regions. Moran et al. (1990) further determined source B to be extragalactic. Figure 3.2 shows the 1667 MHz image of continuum source A alone (NGC 6334 A), this figure is from the same data set that yielded Figure 3.1. Figure 3.3 was made with purely uniform weighting at a resolution of 4.2" × 3.0" in order to examine the small scale structure of NGC 6334 A. In Figure 3.3, the shell structure is resolved while in Figure 3.2 it is not.

The northern and southern lobes have morphologies that are significantly different (Fig. 3.2). The northern lobe is detached from the central shell and vaguely elliptical in shape. The southern lobe is not detached, it appears as an extension to the shell. The southern lobe fans out to the southwest, with a ridge of brighter emission extending due south. These different morphologies hint at different origins for the northern and southern lobes, as described in § 4.1.6 below.



## 3.2 OH Line Data

### 3.2.1 Optical Depths and Column Densities

Optical depth profiles for the 1665 and 1667 MHz OH lines were calculated using the general procedure described in Roberts et al. (1995). We began this process for each OH spectral line with maser-subtracted uv data cubes for each circular polarization (§ 2.2.1). To obtain the highest quality optical depth images, we first removed continuum flux from the uv data cubes with AIPS task UVLSF. This task creates a continuum-subtracted uv data cube and, also, a uv data plane for the radio continuum image. Next we imaged and cleaned the data cubes and data planes for each circular polarization. We took care to define the same boxes in the line cubes as in the continuum planes for the purpose of identifying clean components. In this way, the cleaning process was equivalent in the spectral line data and continuum data, so optical depths (computed from the line-to-continuum ratio) are most nearly correct. Next, we used AIPS task COMB to combine images for the two circular polarizations into Stokes I images, and we used COMB once again to compute optical depths. Before optical depth calculations, the continuum maps were masked to exclude all pixels with continuum brightness less than 0.05 Jy/beam (5% of the peak).

Since OH optical depths in the maps are high, leading to line saturation, we also utilized the limiting optical depth procedure described by Brogan & Troland (2001). In this procedure, an estimate is made of the highest detectable value of  $\tau_{\text{OH}}$  at each individual pixel in the map. This limiting value is based upon the RMS (pixel to pixel) noise in the spectral line maps and upon the continuum brightness at each individual pixel. Obviously, the limiting value of  $\tau_{\text{OH}}$  will be highest for those pixels with the highest continuum brightness. Once these limiting values are established for each pixel, they are applied to the OH optical depth profiles. In particular, any nominal value of  $\tau_{\text{OH}}$  at a given pixel that exceeds the limiting value is replaced by the limiting value. In this way, the  $\tau_{\text{OH}}$  profiles can be used to estimate integrated optical depths, hence,  $N_{\text{OH}}$ , recognizing that  $N_{\text{OH}}$  is a lower limit for pixels with line saturation.

In agreement with Sarma et al. (2000), the OH optical depth profiles for the NGC 6334 complex have components with center velocities in the range  $-2$  to  $-7$  km/s. (We omit from consideration the foreground cloud at  $+7$  km/s, see Sarma et al. 2000). CO and other molecular emission line data (§ 4.1.1) establish that OH components in the range  $-2$  to  $-7$  km/s are associated with the NGC 6334 complex. Our OH optical depth maps for sources other than NGC 6334 A are qualitatively similar to those presented by Sarma et al. (2000). Therefore, we do not discuss these sources any further.

Toward NGC 6334 A, the OH optical depth profiles have several blended components. Optical depth profiles for the 1667 MHz transition are shown in Figure 3.4. These profiles are representative of OH in the northern lobe, the central shell and the southern lobe (top to bottom in the figure). The profiles are similar to those presented by Sarma et al. (2000) although optical depths tend to be higher in the more recent, higher spatial resolution data. Typical 1667 MHz peak optical depths are of order 0.7 near the center of the shell, increasing to 1.5 -2.5 along the edges of the shell. Peak 1667 MHz optical depths in the northern lobe reach  $\approx 1.5$ , while in the southern lobe they reach 2.5 in some places along the east and west edges of the lobe.

The OH column density was determined using the relation

$$N_{\text{OH}}/T_{\text{ex}} = C \int \tau_{\nu} dv \text{ cm}^{-2} \text{ K}^{-1},$$

where  $T_{\text{ex}}$  is the excitation temperature of OH and the constant  $C = 4.1 \times 10^{14}$  and  $2.3 \times 10^{14} \text{ cm}^{-2} (\text{km/s})^{-1}$  for the OH 1665 and 1667 mainlines, respectively (Crutcher 1977). We integrated the optical depth cubes over a velocity range -1.3 to -6.3 km/s. Figure 3.5 shows  $N(\text{OH})/T_{\text{ex}}$  toward source A, derived from the 1667 MHz line and integrated over this velocity range. As noted above, these maps provide lower limits to  $N_{\text{OH}}/T_{\text{ex}}$  for pixels with line saturation.

Figure 3.5 reveals details in the OH distribution significantly beyond those found by Sarma et al. (2000) at lower spatial resolution. OH (by which we mean  $N(\text{OH})/T_{\text{ex}}$ ), is at a minimum near the center of the central shell, and it increases by a factor of three or more along the edges of the shell. Toward the northern lobe, OH is highest along the southern rim. Toward the southern lobe, OH

exhibits intriguing enhancements along the east and west edges of the lobe, defining a “tunnel” of reduced opacity extending southward from the central shell into the southern lobe. This tunnel coincides with a narrow ridge of slightly enhanced radio continuum emission (Fig. 3.2).

### **3.2.2 Kinematics of the OH Gas**

Sarma et al (2001) reported velocity gradients associated with NGC 6334 A for the north-south and for the east-west directions. The north-south velocity gradient might reveal outflow motions associated with the north and south radio continuum lobes. Indeed, the Sarma et al. north-south velocity gradient is in the same sense as that reported in the ionized gas by DePree et al. (1995). However, the magnitude of the velocity gradient is much smaller. An east-west velocity gradient might reveal rotation of the inner region of the molecular torus in that direction.

We have carefully examined the higher spatial resolution OH opacity profiles for signs of velocity gradients. Along the north-south direction, there is certainly a tendency for the line center velocity to increase to the south (Fig. 3.4). However, it is not clear if this effect is a true velocity gradient or merely the result of spatial variations in velocity components at different velocities. In the east-west direction, our data reveal a gradient of  $3.7 \text{ km s}^{-1} \text{ pc}^{-1}$ , consistent with the value  $4.0 \text{ km s}^{-1} \text{ pc}^{-1}$  reported by Sarma et al. As these authors point out, the sense of the OH velocity gradient is the same as that reported by Kraemer et al. 1997 in the larger molecular torus. Finally, there is no trend toward blue-shifted profiles near the center of the central shell. Therefore, OH does not participate in any expansion that the shell may experience.

### **3.2.3 1667/1665 MHz OH Line Ratios**

Under the conditions of local thermal equilibrium (LTE), the ratio of the optical depths of the OH mainlines ( $\tau_{67}/\tau_{65}$ ) is 9/5. We find that the observed line ratio is always less than this thermal value toward NGC 6334 A. The ratio is typically 1.0 over NGC 6334 A, with values  $\approx 1.3$ – $1.4$  in selected directions toward the edge of the central shell source. Therefore, there is an overpopulation of the F=1 level compared to the F=2 level of the lower-energy  $\Lambda$

doublet. These findings are consistent with results presented in Brooks and Whiteoak (2001). Non-LTE optical depth ratios are also found in OH absorption toward other continuum sources including Orion A, S106, M17 and Orion B.

### 3.3 Magnetic Field Determination

To calculate the magnetic field strengths using the Zeeman effect, we fit a numerical derivative of the Stokes I spectrum to the Stokes V spectrum for each pixel in the data cubes with significant I and V signal. This process is described by Roberts et al. (1993). The fits yield values for  $B_{\text{los}}$  and estimates of the  $1-\sigma$  errors in these values from 1665 and 1667 MHz lines independently. In the NGC 6334 complex we find significant magnetic field detections only toward NGC 6334 A.

Figure 3.6 shows the 1665 and 1667 MHz Stokes I and V profiles at a position toward the central shell source of NGC 6334 A. Superimposed upon each V profile is the derivative of the corresponding I profile, scaled to the fitted field value. At this position, we find  $B_{\text{los}} = 600 \pm 100 \mu\text{G}$  in the 1665 MHz line and  $540 \pm 110 \mu\text{G}$  in the 1667 MHz line. Note that these values are consistent with each other despite the fact that the Zeeman coefficients for the two lines are significantly different (3.27 and 1.96 Hz/ $\mu\text{G}$  for the 1665 and 1667 MHz lines, respectively). This consistency establishes the reality of the Zeeman effect detected in the two OH lines. Values of  $B_{\text{los}}$  derived in this study are about a factor of two higher than the ones derived by Sarma et al. (2000), very likely an effect of the increased spatial resolution. Examination of the V profiles in Figure 3.6 reveals that our OH maser subtraction process (§ 2.2.1) has not been successful in eliminating maser-induced circular polarization, especially in the 1665 MHz line. Fortunately, maser emission is largely confined to velocities more negative than those of the thermal OH absorption lines. All values for  $B_{\text{los}}$  were fit over the velocity range -6.3 to 4.1 km/s in order to exclude velocity channels affected by the masers.

Examination of the V profiles in Figure 3.6 also reveals an offset between the Zeeman-related features and the fitted derivative curves. For both OH lines, the Zeeman-related V features are shifted to higher velocity relative to the

derivative curves. Careful visual examination of optical depth profiles at pixels where  $B_{\text{los}}$  is detected appears to reveal at least two highly blended velocity components. One is centered near -2.7 km/s, the other near -3.8 km/s. There is a hint of this behavior in the 1667 MHz I profile of Figure 3.6b. We suspect that the Zeeman effect detected at the pixel of Figure 3.6 (and elsewhere) arises preferentially in the -2.7 km/s OH velocity component. We tried some simple experiments with Gaussian fitting of the I profiles. Next we computed the derivative of a Gaussian component centered near -2.7 km/s and scaled it to match the Zeeman-related features in the V profiles of Figure 3.6. These experiments confirmed that the Zeeman features in the V profiles can arise from a velocity feature centered near -2.7 km/s. However, the implied field strengths from these Gaussian fitting experiments are not qualitatively different from those derived in the usual way. Also, the fit of Gaussian components of the I profiles is often uncertain owing to blending between components and insufficient sensitivity in these profiles. We conclude that the standard fitting procedure involving the derivative of the observed I profiles is adequate to reveal the astrophysically significant magnetic field information in the data.

### 3.3.1 Spatial Variations of Magnetic Fields toward NGC 6334 A

In Figure 3.7 we show a map of  $B_{\text{los}}$  (colors) across much of the central shell source of NGC 6334 A with continuum contours superimposed. This map is derived from a combination of the independent values of  $B_{\text{los}}$  derived from the two OH lines. At each pixel we compute an average of  $B_{\text{los}}$  (1665 MHz) and  $B_{\text{los}}$  (1667 MHz), weighted by the inverse squares of the  $1-\sigma$  errors for each. We also estimate the  $1-\sigma$  error of the average  $B_{\text{los}}$  at each pixel. Values of  $B_{\text{los}}$  in Figure 3.7 are only shown where they exceed two times the  $1-\sigma$  errors. Overlaid on the map of  $B_{\text{los}}$  are 1667 MHz continuum contours for the central shell source. Also shown is an ellipse representing the synthesized beamwidth of the Zeeman effect data.

Figure 3.7 contains at least 8 independent resolution elements. All values of  $B_{\text{los}}$  are positive, that is, the field points away from the observer. The figure shows  $B_{\text{los}} \approx 200 \mu\text{G}$  across the central and much of the northeastern part of the

shell source. Along the north edge of the shell source,  $B_{\text{los}}$  rises to at least 700  $\mu\text{G}$ . No fields at the  $2\text{-}\sigma$  significance level or higher were detected in the southwestern sector of the shell source, although  $V$  profiles in this region of the map do often show weak Zeeman signatures having the same positive sign of the field toward other parts of the central shell source.

## 4. Discussion

### 4.1 The Nature of NGC 6334 A and its Lobes

Radiation from NGC 6334 A has been observed at many wavelengths. These include radio continuum emission from the ionized gas (§ 1.2.1, Figures 4-6), radio spectral lines and dust continuum emission from the molecular core, and near and mid-IR radiation from stellar objects and diffuse material. Information obtained from these observations yields important clues to the nature of the NGC 6334 A molecular core/UCHII region.

#### 4.1.1 Molecular Gas in the NGC 6334 A Region

The distribution of molecular gas in NGC 6334 A is revealed from radio spectral line studies, including OH absorption reported here. Kraemer et al. (1997) reported a rotating molecular torus with  $M \approx 2000 M_{\text{solar}}$  and  $n \approx 3 \times 10^3 \text{ cm}^{-3}$ . They suggested that this torus was responsible for the northern and southern lobes (§1.2.1). Kraemer et al. also observed  $\text{NH}_3$  (3, 3) emission at much higher spatial resolution. They found several small (0.1 pc) clumps of gas along the rim of the central shell HII region, with the most prominent one along the northeast rim of the shell. They also identified other  $\text{NH}_3$  cores immediately to the west of the shell. Other spectral line studies of NGC 6334 A include those of De Pree et al. ( $\text{H}_2\text{CO}$ , 1995) and Sandell ( $\text{H}^{13}\text{CO}^+$ , 1999).

To further study the distribution and kinematics of molecular gas in the NGC 6334 A region, we have made use of James Clark Maxwell Telescope (JCMT) archival data for the 342 GHz, SiO J=7-6 line (Half Power Beam Width  $\sim 14''$ ) and 850 micron continuum emission. In Figure 3.8 we show the integrated SiO line strength (colors) with 850  $\mu\text{m}$  continuum contours overlaid. We take the latter to be approximately representative of  $N(\text{H}_2)$ , assuming a constant gas-to-dust ratio and temperature, and assuming that the continuum emission is

predominantly from dust. The continuum contours delineate a molecular core of dimensions  $0.2 \times 0.4$  pc (to half power), that is, about five times smaller than the molecular torus of Kraemer et al. (1997). (See Sandell 1999 for previous maps of dust continuum emission from the NGC 6334 A region.) It is clear from Figure 3.8 that the SiO line and 850 micron continuum emission are distributed in very similar ways. Also, we have carefully compared the SiO emission line profiles with OH opacity profiles at representative positions toward the central shell. We find very good agreement in line shape and center velocity, suggesting that SiO emission and OH absorption sample similar regions in the molecular core. This agreement extends to the east-west velocity gradient identified in the OH absorption (§3.2.2). Finally, we computed an average SiO profile for which we find  $\Delta v_{\text{FWHM}} = 4.4 \text{ km s}^{-1}$ . This value provides an accurate estimate of the velocity dispersion in the molecular core.

We have estimated physical parameters for the molecular core from the 850  $\mu\text{m}$  continuum brightness. To do so, we estimate  $N(\text{H})$  from the 850  $\mu\text{m}$  continuum emission using the grain optical depth per hydrogen atom,  $C_\lambda$  calculated by Cloudy (Ferland et al. 1998.) This code applies Mie theory to a representative distribution of grain sizes assumed to contain Si and graphite particles. The result is  $C_\lambda = 8 \times 10^{-27}$  at 850 microns. Therefore,  $N(\text{H}) = \tau_d / C_\lambda$ , where  $\tau_d$  is the dust optical depth. From the Rayleigh-Jeans approximation to the Planck law  $\tau_d \propto B_{850} / T_d$ , with  $B_{850}$  the 850 micron brightness and  $T_d$  the dust temperature. For convenience, we convert  $N(\text{H})$  to its equivalent visual extinction  $A_v$  using  $A_v / N(\text{H}) = 5.3 \times 10^{-22} \text{ mag cm}^2$ . In Figure 3.9 we show the 850 micron dust emission, scaled to  $A_v$  if  $T_d = 100 \text{ K}$  (gray scale and blue contours), and the 1667 MHz continuum (red contours). The peak  $A_v \approx 600 \times (100 / T_d)$ , so  $N(\text{H}) = 1.0 \times 10^{24} \text{ cm}^{-2} \times (100 / T_d)$ . For a mean radius of 0.3pc, the implied core mass is  $900 \times (100 / T_d) M_{\text{solar}}$  with an average  $n \approx 2 \times 10^5 (100 / T_d) \text{ cm}^{-3}$ . For  $T_d \approx 100 \text{ K}$ , this mass is very close to the median mass found by Shirley et al. (2003) for 63 high-mass star-forming cores mapped in the CS J=5-4 line. Also, the mean radius of the NGC 6334 A molecular core (0.3 pc, see above) is close to the median value determined by Shirley et al. for their sample. Evidently, the NGC

6334 A molecular core, as delineated by its 850 micron dust emission, is very typical of high-mass star-forming cores. The core, in turn, lies within a more extended envelope of lower-density molecular gas mapped out by Kraemer et al. (1997).

The molecular core mass computed from the 850 micron continuum emission may be compared with the virial mass estimated from the core radius (0.3 pc) and FWHM velocity width ( $4.4 \text{ km s}^{-1}$ ), the latter taken from the average SiO emission profile. We use the formulation of Wolkovitch et al. (1997), equivalent to that of Shirley et al. (2003), and we take a power law density relationship  $n \propto r^{-p}$  with  $p \approx 1.75$ , a typical value (see Mueller et al. 2002). We find  $M_{\text{vir}} \approx 900 M_{\text{solar}}$ , equivalent to the value we estimated from the dust continuum emission with  $T_d = 100 \text{ K}$ . The NGC 6334 A molecular core is close to virial equilibrium if  $T_d = 100 \text{ K}$ . If  $T_d < 100 \text{ K}$ , then the cloud is not supported by internal motions alone. Of course, such a circumstance would naturally arise if part of the core's internal support arose from magnetic fields.

The 1665 and 1667 MHz OH opacities (spatial resolution 0.05 pc) also provide useful information about molecular gas in the NGC 6334 region. (See, also, §3.2.1.) First, there is no evidence for blue-shifted OH gas toward the center of the central shell (Fig. 3.4). We conclude that the molecular gas traced by OH is not part of an expanding shell. The map of integrated 1667 MHz opacity (Fig. 3.5) reveals enhanced OH optical depths along the rim of the central HII shell, with a minimum opacity centered very near the location of IRS 19 (Harvey, Hyland & Straw 1987). Radiation from IRS 19 may be warming and disassociating OH closest to the star, resulting in a localized minimum in OH opacity. The OH opacity minimum extending to the south coincides with the ridge of enhanced radio continuum emission and, also, with a maximum in the 3.3 micron Polycyclic Aromatic Hydrocarbon (PAH) band observed by Burton et al. (2000). In Figure 3.10 we present contours from the 3.3 micron Burton et al. map superimposed upon the 1667 MHz OH continuum radiation. The 3.3 micron emission in the southern lobe has a cometary appearance, with the head of the "comet" coinciding with the ridge of enhanced radio continuum emission.



Moreover, the “comet” fits neatly within the OH opacity minimum, suggesting some process that simultaneously reduces OH opacity and increases emission in the 3.3 micron PAH band. We discuss this possible process in § 4.1.6.

The significant enhancement in OH optical depth toward the edges of the continuum source (§ 3.2.1 and Fig.3.5) may arise if the absorbing molecular gas lies primarily in a thin layer just outside the ionized gas. Moreover, molecular gas surrounding the central shell has no radial motion since OH absorption lines toward its center (§ 3.2.1) show no sign of blue or red shift relative to the lines near the edges of the shell.

#### **4.1.2 The Central Shell**

The central shell of ionized gas is very comparable in diameter to the molecular core revealed by 850 micron dust emission (see Fig. 3.9). The density of the central shell is estimated to be  $n \approx 2 \times 10^4 \text{ cm}^{-3}$ , with a total mass of about  $0.4 M_{\text{solar}}$  (Carral 2002). Moreover, the central shell must lie behind a significant column density of gas. No indication of the shell appears in the 12.5 or 20.5 micron images of NGC 6334 A (Kraemer et al. 1999), despite the fact that hot dust in the shell should emit strongly at these wavelengths. (See Hoare et al. 1991). If the shell lies behind most of a 100 K molecular core, then  $A_v \approx 600$  (§4.1.1). In such a case, the 20 micron extinction is about 17 mags since  $C_v/C_{20\mu\text{m}} \approx 35$  according to Cloudy (§4.1.1). Such a 20  $\mu\text{m}$  extinction is sufficient to strongly attenuate emission of the shell.

The shell-like nature of the central radio continuum source suggests the existence of a wind-blown bubble of ionized gas (§1.2.1). Such bubbles develop after a short initial phase of expansion at the stellar wind velocity. The system then evolves into an x-ray emitting hot bubble filled by shocked stellar wind material and interstellar gas. The bubble is surrounded by a thin dense shell formed by most of the swept-up cloud matter (Shull 1980). Carral et al. (2002) suggest that density gradients in molecular cores surrounding the NGC 6334 A shell could affect the evolution of the expanding bubble by fragmenting the shell structure and reducing the expansion rate. Such hot bubble structures have been observed in x-ray wavelengths in the M17 and S106 star-forming regions.

Sekimoto et al. (2000) have performed observations of hard x-ray emission toward NGC 6334. They propose a model in which a high-temperature plasma originates from interactions between stellar winds from massive stars and the molecular cloud. Aviles, Lizano & Raga (2005) have considered the evolution of HII regions inside hot molecular cores. They find that the expansion of the HII region is driven by the momentum of a stellar wind, leading to a thin shell of hot shocked stellar wind material surrounded by a thin shell of swept up and ionized material from the molecular cloud. Surrounding the HII region, of course, is the molecular gas that has yet to be dissociated and ionized.

#### **4.1.3 The Nature of the Central Exciting Source**

The symmetric nature of the central shell of radio continuum emission suggests that an exciting star or stars must lie close to its center. RCM82 estimate that an O7.5 ZAMS star can provide the ionization implied by the 6 cm radio continuum flux they observed. Our 18 cm radio flux is compatible with this estimate. It is possible that such a star is responsible for the 3.5 cm radio point source observed near the center of the shell by Carral et al. (2002, §1.2.1). Quite unlikely, however, is the possibility that IRS 19 (also known as KDJ-2) is the exciting source, as suggested by Burton et al. (2000). IRS 19 lies near the southeastern edge of the central shell, quite far from its center. Also, Harvey, Hyland & Straw (1987) argue that IRS 19 does not have near-IR colors consistent with a reddened O7.5 ZAMS star.

It is straightforward to explain why the exciting source for the central shell is invisible in the near-IR. The deepest available near-IR image of NGC 6334 A (K-band, 2.2 microns, Persi, Tapia & Roth 2000) shows no indication of such a stellar object close to the center of the shell. We estimate that the exciting source of the shell would be undetectable in the K-band image of Persi et al. if  $m_K > 17.5$  mag. Moreover,  $M_V$  for an O7.5 ZAMS star is estimated to be -4.77 (Vacca et al. 1996), and V-K is -0.93 (Koornneef 1983). Therefore, we expect such a star to have  $m_K = 7.3$  mag at the distance of 1.7 kpc, so its K-band extinction must be at least 10.2 mag if it is undetectable. The Cloudy-derived values for  $C_\lambda$  (§ 4.1.1) have  $C_V/C_K \approx 8.6$ , so an O7.5 ZAMS star will be invisible in

the near-IR image if  $A_v > 8.6 \times 10.2 \approx 90$  mag. This  $A_v$  value is a small fraction of the 600 mag through the molecular core estimated above from the 850  $\mu\text{m}$  dust continuum radiation. In short, the exciting star for the NGC 6334 A central shell would not be visible in the deep K-band image of Persi et al. unless it lay rather close to the near side of the molecular cloud.

#### 4.1.4 The Northern Lobe

The northern and southern lobes of NGC 6334 A radio continuum emission have been described as part of a biconical or bipolar HII region in which radiation and possibly material escapes preferentially along the poles of a confining neutral disk (§ 1.2.1). RCM88 first suggested this model, concluding that the radio continuum emitted by the lobes arises from gas ionized in place by ionizing photons escaping from the central star or stars. The model assumes that there are breaks in the central ionized shell through which ionizing stellar radiation escapes, and these breaks are oriented north and south. Breitschwerdt & Drury (1991) developed a general model for the evolution of bipolar ionization cones and applied it to NGC 6334 A. The biconical model was also cited by DePree et al. (1995) in their analysis of radio recombination line velocities from NGC 6334. The northern and southern radio continuum lobes have their counterparts in the near-IR (Harvey, Hyland & Straw 1987; Persi, Tapia & Roth 2000; Burton et al. 2000) and in the mid-IR (Kraemer et al. 1999). It is not clear *a priori* that the material responsible for radio continuum emission is the same as that responsible for the near and mid-IR emission.

On morphological grounds, however, the northern radio continuum lobe is almost certainly *not* part of a biconical HII region excited by a source in the central shell. First, the northern lobe appears detached from the central shell (§ 3.1). Second, the gap in radio continuum emission that separates the northern lobe from the central shell coincides with an enhancement in 3.3 micron PAH emission. (See Fig. 3.10.) Also, the PAH emission appears to trace out a partial shell about the northern lobe of radio continuum emission. This morphology can be understood in light of the study of Sellgren, Tokunaga & Nakada (1990). These authors observed various tracers along the edge-on ionization front of the

Orion nebula. They found that the 3.3  $\mu\text{m}$  emission fits neatly between emission attributed to ionized and molecular gas. That is, the 3.3  $\mu\text{m}$  emission appears to be a PDR (i.e.  $\text{H}^0$ ) tracer. More recently, Kassis et al. (2006) found further evidence that PAH emission in Orion peaks just outside the HII region. We suggest that a similar phenomenon occurs with the northern lobe of NGC 6334 A. In this case, the ionized gas of the northern lobe is surrounded by PAH emission fluorescently excited by far-UV radiation escaping from the northern lobe HII region. (See, also, Burton et al. 2000.) Finally, we note that the center velocity of the  $\text{H}92\alpha$  radio recombination line toward the northern lobe ( $-4.7 \pm 0.2$   $\text{km s}^{-1}$ , De Pree et al. 1995) is virtually identical to that of the principal velocity component in the OH opacity profile toward the lobe (Fig. 3.4, upper profile). This similarity is inconsistent with the northern lobe as an outflow from the central shell unless the flow is very nearly in the plane of the sky.

If the northern lobe is truly a separate HII region, then IRS 54 is a likely candidate for the exciting star. IRS 54 is the brightest near-IR source in the northern lobe (Harvey, Hyland & Straw 1987, Persi, Tapia & Roth 2000), and it is located close to the peak radio continuum brightness of the lobe. The 18 cm radio continuum flux of the northern lobe is consistent with an O9.5 ZAMS star. Taking  $M_V = -4.3$  mag for such a star from Vacca et al. (1996) and near-IR colors from Koornneef (1983), we find that the observed values of  $m_J$  and  $m_K$  (Harvey, Hyland & Straw 1987) are consistent with a O9.5 ZAMS star having  $A_V = 17$  mag. Moreover, the 850 micron map scaled to  $A_V$  (Fig. 3.9) suggests that  $A_V \approx 20$  in the direction of IRS 54, consistent with this scenario.

#### **4.1.5 The Southern Lobe of Radio Continuum Emission**

The nature of the southern lobe is likely to be quite different from that of the northern lobe. An important indication of this difference lies in the velocity of the ionized gas in the southern lobe. De Pree et al. (1995) report an  $\text{H}92\alpha$  velocity of  $11.5 \pm 0.5$   $\text{km s}^{-1}$  for the southern lobe, a velocity 10-15  $\text{km s}^{-1}$  *redshifted* from other velocities of ionized and neutral gas in the region. The clear implication is that the southern lobe (unlike the northern lobe) is receding from the molecular core at about the sound speed in the ionized region. This

behavior is expected if the ionized gas is escaping into a low density medium. The outflow may be related to the gap in the central shell toward the south (§1.2.1), a gap which could mark the escape route for ionized material flowing out into the southern lobe. Also marking the escape route may be the tunnel-like minimum in  $\tau_{\text{OH}}$  along with the ridge of enhanced radio continuum emission superimposed upon the  $\tau_{\text{OH}}$  minimum (§4.1.1 and Fig. 3.5).

Unlike the case for the northern lobe, the morphology of the southern lobe is distinctly different in radio continuum emission compared to near and mid-IR emission. The cometary appearance of the 3.3 micron PAH emission (§4.11, Fig. 3.10) is also found in the K-band images of Harvey, Hyland & Straw (1987) and Persi, Tapia & Roth (2000), and the head of the “comet” is clearly visible in the 12.5 micron image of Kraemer et al. (1999). Yet this cometary morphology is not found in the southern radio continuum lobe. It is unlikely that the difference in morphologies is a result of differential extinction. First, we know the morphology of the extinction from the 850 micron dust continuum map (Fig. 3.9). It bears no connection to the cometary shape of the IR emission. Second, the cometary morphology is very similar from J-band to 12.5 microns despite more than an order of magnitude difference in extinction expected over this wavelength range ( $C_J \approx 11 C_{12\mu}$  from the Cloudy extinction models). We conclude that the material responsible for the near and mid-IR emission in the southern lobe is not primarily the ionized gas responsible for the radio continuum emission. It is quite possible that the material responsible for near and mid-IR emission there is unrelated to the ionized gas responsible for the radio continuum emission.

#### **4.1.6 A Model for the NGC 6334 A Region**

The OH opacity data in the present study, together with dust continuum maps, radio spectral line data and IR maps, suggest a model for the overall nature and geometry of the NGC 6334 molecular core and UCHII region. This model is illustrated in the cartoon of Figure 3.11. We envision a massive ( $\approx 1000 M_{\text{Solar}}$ ), somewhat elongated molecular core with  $n \approx 10^5 \text{ cm}^{-3}$  and diameter  $\approx 0.3 \text{ pc}$  embedded within a lower density molecular envelope of comparable mass and about five times larger dimensions (hence, about a factor 100 lower density).

The core is typical of those observed by Shirley et al. (2003) that are associated with high-mass star formation. Within this core, at least one O7.5 ZAMS star has formed and created a shell-like UCHII region (shown in orange in Fig. 3.11). The UCHII region may have developed along the lines of models described by Aviles, Lizano & Raga (2005) in which the stellar wind-driven ionized gas expands beyond the boundary of the molecular core in  $t \leq 5 \times 10^4$  yr. Since the shell of ionized gas is now nearly as large in diameter as the molecular core, the shell is beginning to break out of the molecular core, creating a champagne flow to the south. The  $\approx 10 \text{ km s}^{-1}$  redshift of the ionized gas in the southern lobe is best explained if the champagne flow is passing through an opening on the back side of the core. That is, the UCHII region lies behind most of the molecular core, hidden by several 100 magnitudes of visual extinction. Therefore, the exciting star and all near and mid-IR emission from the central shell and its PDR are invisible.

The southerly escape path of the champagne flow is clearly marked by tracers of ionized, PDR and molecular gas. The ionized gas is responsible for the ridge of enhanced radio continuum emission in the southern lobe. (The ridge appears as a small red peak south of the central shell in Fig. 3.10.) Immediately surrounding this outflow of ionized gas to the south is a PDR marked by the cometary shaped southern  $3.3 \mu\text{m}$  emission (and radiation at other IR wavelengths). The cometary structure is visible to us in the IR because it lies mostly south of the molecular core and suffers, as a result, much less extinction ( $A_v < 50 \text{ mag}$ , so  $A_K < 6$ , see Fig. 3.9) than radiation from the central shell. Moreover, radiation from the ionized gas is heating and dissociating molecular gas along the escape path, creating the southward-directed minimum in OH opacities (Fig. 3.5). The slight redshift ( $\approx 2 \text{ km s}^{-1}$ ) of the southern lobe OH profile relative to that of the central shell probably indicates that the molecular gas has been partially entrained by the outflowing ionized gas. Such entrainment would be natural in a magnetized medium since the magnetic field dynamically couples gas in adjacent regions. Note that the champagne flow cannot be flowing directly away from the viewer, as if the central shell were really a

hemisphere facing backwards. This conclusion arises from the fact that the H92 $\alpha$  line center velocity toward the central shell is only slightly redshifted ( $\approx 2$  km s $^{-1}$ ) relative to the systemic velocity of the molecular core as defined by the SiO emission. Therefore, the back side of the shell must still be mostly intact. So the escape path for the champagne flow is directed mostly southward rather than directly backward, as shown in Figure 3.11.

Coincidentally, an independent HII region has formed north of the molecular core where the extinction is also relatively low. This HII region is excited by a later type star that appears as IRS 54. Surrounding the northern HII region is a partial shell of neutral gas, a PDR, traced out by the 3.3 micron PAH emission. Molecular gas also lies along this line-of-sight, as evidenced by the OH opacity profile toward the northern lobe. The northern lobe appears superficially to be the northern extension of a biconical HII region. But this appearance is only an illusion.

#### **4.2 Magnetic Effects in the NGC 6334 A Region**

The importance of the magnetic field in the NGC 6334 A region depends upon the balance between magnetic and other relevant energies, especially the gravitational energy and the energy of internal motions. (Thermal energy is usually insignificant in the ISM except in the most quiescent regions of molecular cores.) A related issue is the question of what regions of the molecular cloud are sampled by the OH Zeeman effect.

The regions sampled by the OH Zeeman effect are somewhat difficult to assess since OH is a reactive molecule subject to a number of formation and destruction processes. The most straightforward assumption about OH sampling is that the molecule samples the NGC 6334 core in a manner similar to other common molecular emission line tracers such as C $^{18}$ O. The similarities between the SiO J=7-6 emission line profiles and the OH optical depth profiles (§ 4.1.1) suggest that this assumption is reasonable. Moreover, we argue the central shell providing the continuum radiation absorbed by OH lies near the far side of the molecular core (§ 4.1.6). If so, then the OH absorption can arise virtually anywhere in the core. Also, Troland et al. (1996) find that the OH and C $^{18}$ O

emission line profiles toward the Rho Oph molecular cloud core are virtually identical in shape. This similarity suggests that the two molecules sample the same regions of that particular cloud, although both molecules are likely depleted in the interior of the cloud. Of course, the NGC 6334 A molecular core is quite different from its Rho Oph counterpart since the former is the site of massive star formation while the latter is not. Therefore, the stellar radiation field near the NGC 6334 A is quite different, and it includes radiation capable of disassociating OH and other molecules. In such an environment, OH may exist primarily in a thin layer close to the PDR created by the stellar radiation field. Such a locale may be suggested by the tendency of  $\tau_{\text{OH}} \propto N_{\text{OH}}/T_{\text{ex}}$  to increase along the edges of the central shell and along the edges of the escape path of ionized gas that makes up the southern lobe, that is, in the locales most likely to be exposed to dissociating radiation. Viti, Hartquist & Myers (2006) modeled the abundance of OH in regions of massive star formation with the primary motivation of establishing the location of the Zeeman-sensitive OH. They considered a scenario in which stellar radiation penetrating a molecular cloud first evaporates ices off grain mantles, freeing molecules like H<sub>2</sub>O into the gas phase. Next the H<sub>2</sub>O is disassociated to form OH; finally, the OH itself is disassociated. Therefore, OH is only abundant in a narrow zone of the PDR, with the details quite dependent upon the specific parameters of the various models they run. If OH exist primarily in such narrow zones in the NGC 6334 A region, then we conclude that it will be very difficult to establish the detailed physical parameters of those zones on theoretical grounds. However, such details may not be crucial to a Zeeman effect study such as this one. If the process of creating OH in the PDR does not otherwise disturb the gas (hence, alter its density), then the locales sampled by OH absorption, however narrow, may still be representative of the molecular core itself. In such a case the OH Zeeman effect provides a reasonable measure of the magnetic field in the undisturbed core.

We now undertake an analysis of the energetics of the NGC 6334 A molecular core assuming that the OH Zeeman effect provides a reasonable estimate of its magnetic field strength. This analysis is similar to that reported by



Abel et al. (2006) for the Orion Veil region. For the purpose of this analysis, we adopt the following parameters for the NGC 6334 A molecular core: We take  $B_{\text{tot}} = 1$  mG, based upon the peak  $B_{\text{los}} \approx 600$   $\mu\text{G}$  measured by the OH Zeeman effect (Fig. 3.6). We take  $\Delta v_{\text{FWHM}} = 4.4$   $\text{km s}^{-1}$ ,  $n_{\text{H}} = 2 \times 10^5$   $\text{cm}^{-3}$  and  $N_{\text{H}} = 1 \times 10^{24}$   $\text{cm}^{-2}$  (§ 4.1.1). Furthermore, we assume  $T_{\text{K}} = 100$  K. With these parameters (table 3.2), we can compute the same parameters of core energetics computed for Orion by Abel et al. (2006). We find that the *turbulent* Mach number  $m_{\text{S}} \approx 4$ . That is, the internal motions responsible for the SiO line width are highly supersonic. Note that  $m_{\text{S}}^2$  is the ratio of turbulent to thermal energy densities, so we conclude that thermal energy in the NGC 6334 A molecular core is insignificant compared to turbulent energy density, a property of almost all molecular clouds and all but the most quiescent molecular cores. One can also define a *magnetic* Mach number  $m_{\text{A}}$  such that  $m_{\text{A}}^2$  is the ratio of turbulent to magnetic energy densities. For the adopted NGC 6334 A molecular core parameters, we find  $m_{\text{A}} \approx 0.6$ , suggesting that magnetic energy density is comparable to turbulent energy density. This circumstance is referred to as *magnetic equipartition* (equivalent to having the turbulent velocity comparable to the Alfvén velocity). Magnetic equipartition is expected if the observed turbulent motions in a magnetized cloud are not true turbulence but manifestation of transverse Alfvén waves. Finally, we use the estimated value of  $N_{\text{H}}$  for the NGC 6334 molecular cloud to estimate  $\lambda$ , the ratio of the magnetic field to the critical magnetic field necessary to provide support for the core against gravity (see Crutcher 1999). This ratio is a measure of the ratio of gravitational to magnetic energy in the molecular core. From Crutcher (1999) we have  $\lambda \approx 0.5 \times 10^{-20} N_{\text{H}}/B$  where  $N_{\text{H}}$  is in  $\text{cm}^{-2}$  and  $B$  is the magnetic field in  $\mu\text{G}$ . For the NGC 6334 A molecular core, we have  $\lambda \approx 5$ , suggesting that magnetic energy is rather smaller than gravitational energy in the core. If so, then the core is said to be *magnetically supercritical*. That is, magnetic energy cannot support the cloud against self-gravitation, the internal support of the cloud comes, presumably, from the internal motions responsible for the observed SiO and OH line widths. This latter condition, of course, represents classical virial equilibrium as

discussed in § 4.1.1. The conclusion that the NGC 6334 A molecular cloud is magnetically supercritical, of course, is tentative, if likely. A combination of higher  $B_{\text{tot}}$  than assumed above (i.e. higher than 1 mG) and higher temperature (thereby reducing the estimated value of  $N_{\text{H}} = 1 \times 10^{24} \text{ cm}^{-2}$ ) could yield a value of  $\lambda$  closer to unity.

TABLE 3.1  
OBSERVATIONAL PARAMETERS FOR VLA OBSERVATIONS

Parameter	OH
Date.....	October 10 <sup>th</sup> , 1999
Configuration.....	BnA
R.A. of field center (J2000).....	17 <sup>h</sup> 17 <sup>m</sup> 00.0 <sup>s</sup>
Decl. of field center (J2000).....	-35°45'00.0"
Total Bandwidth (MHz).....	0.19
Number of Channels.....	128
Hanning smoothing.....	No
Channel Spacing (km/s).....	0.27
Approximate time on source (hr)...	6
Rest Frequency (MHz).....	1665.402 1667.359
FWHM of synthesized beam.....	9".1x5".5 8".2x5".0
RMS noise (mJy/beam).....	
Line channels.....	9
Continuum.....	6

TABLE 3.2  
NGC 6334 SOURCE A PARAMETERS

Parameter	Value
Radius (r).....	0.3 kpc
Mass (M).....	1000 $M_{\text{sun}}$
N(H).....	$1 \times 10^{24} \text{ cm}^{-2}$
$n_p$ .....	$2 \times 10^5 \text{ cm}^{-2}$
$T_k$ .....	100K
$\Delta U$ .....	4.4 km/s
$B_{\text{los}}$ .....	600 $\mu\text{G}$

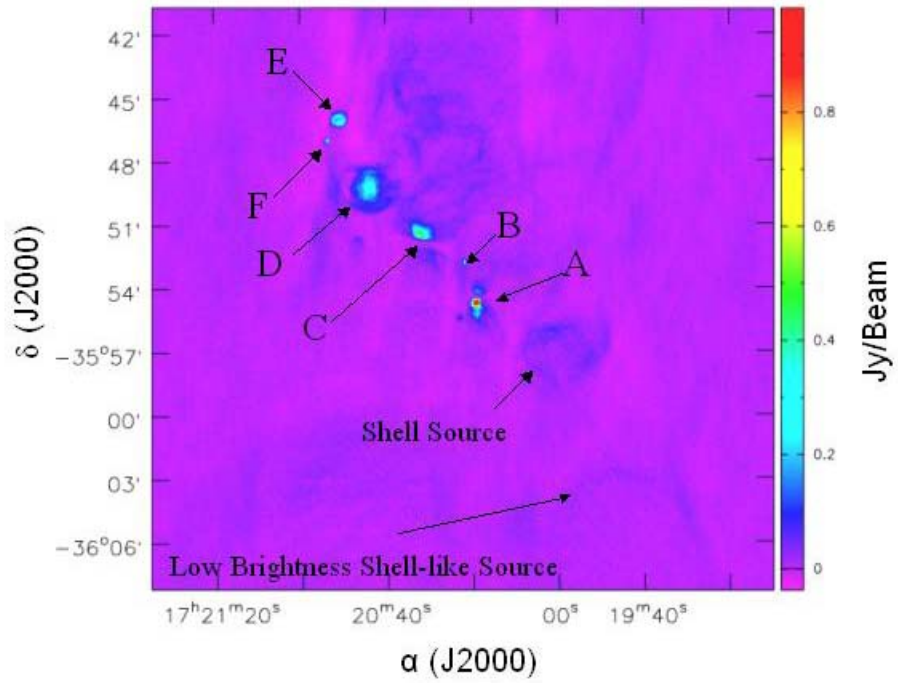


Fig. 3.1 -18cm continuum map of the NGC 6334 Complex at 1667 MHz. The beam is  $8''.2 \times 5''.0$ .

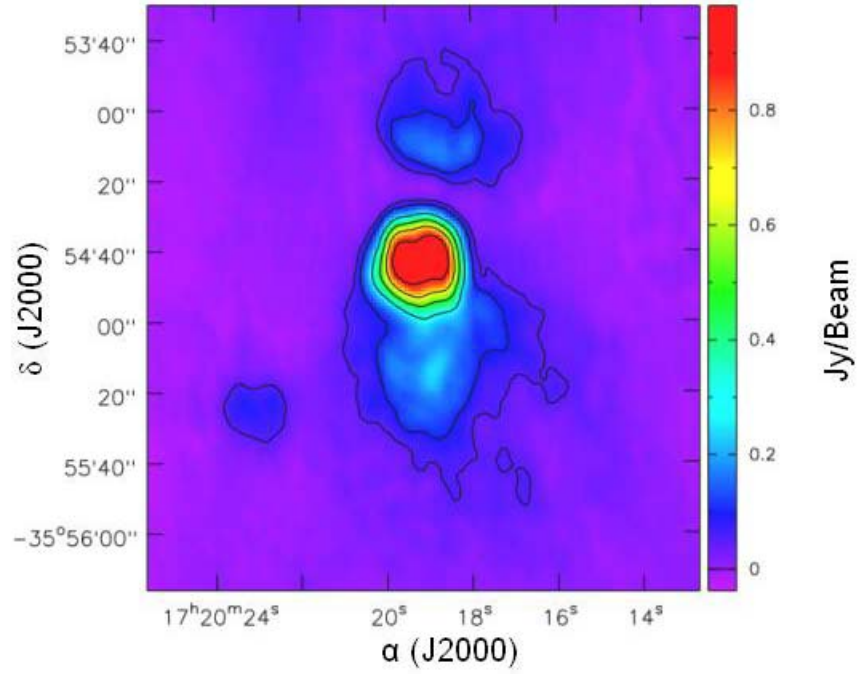


Fig. 3.2 -18cm continuum map of NGC 6334 source A at 1667 MHz. Contour intervals are at 0.05, 0.1, 0.3, 0.5, 0.7, 0.9 of the peak continuum flux of 0.98 Jy/beam. The beam is  $8''.2 \times 5''.0$ .

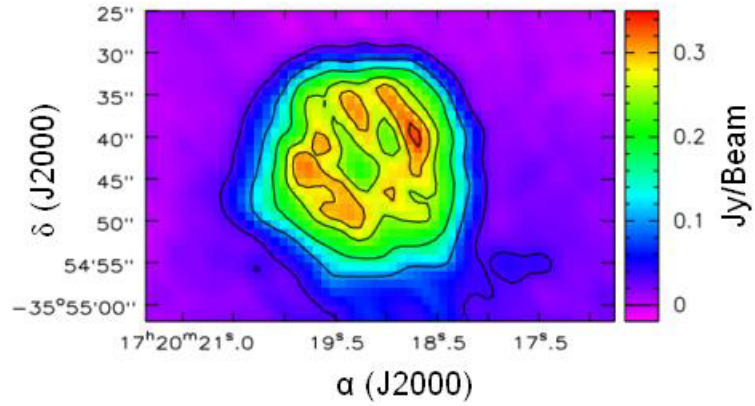


Fig. 3.3 -18cm continuum map of NGC 6334 source A at 1667 MHz. Contour intervals are at 0.1, 0.3, 0.5, 0.7, 0.8, and 0.9 of the peak continuum flux of 0.36 Jy/beam. The beam is 4"x3"; the image has been made at a higher resolution by uniformly weighting the data.

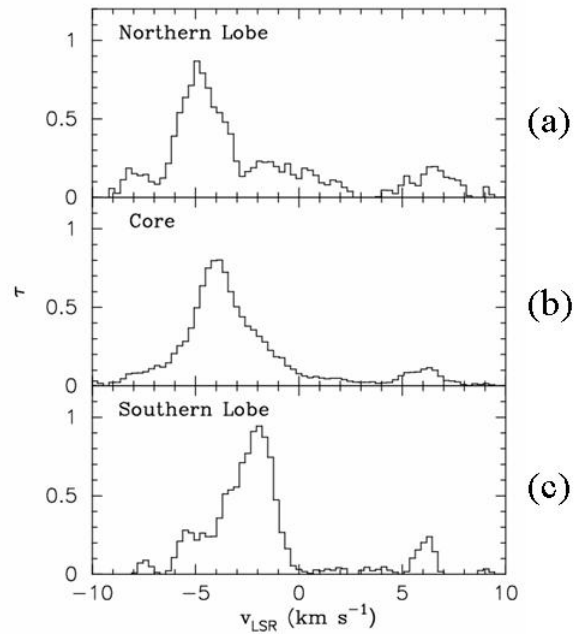


Fig. 3.4 -OH 1667 MHz optical depth profile toward (a) the northern lobe of source A at  $\alpha=17\text{h}20\text{m}19\text{s}.1$ ,  $\delta=-35^\circ54' 8''.9$ ; (b) the core of source A at  $\alpha=17\text{h}20\text{m}19\text{s}.1$ ,  $\delta=-35^\circ54'41''.9$ ; (c) the southern lobe of source A at  $\alpha=17\text{h}20\text{m}19\text{s}.1$ ,  $\delta=-35^\circ54'59''.9$ .



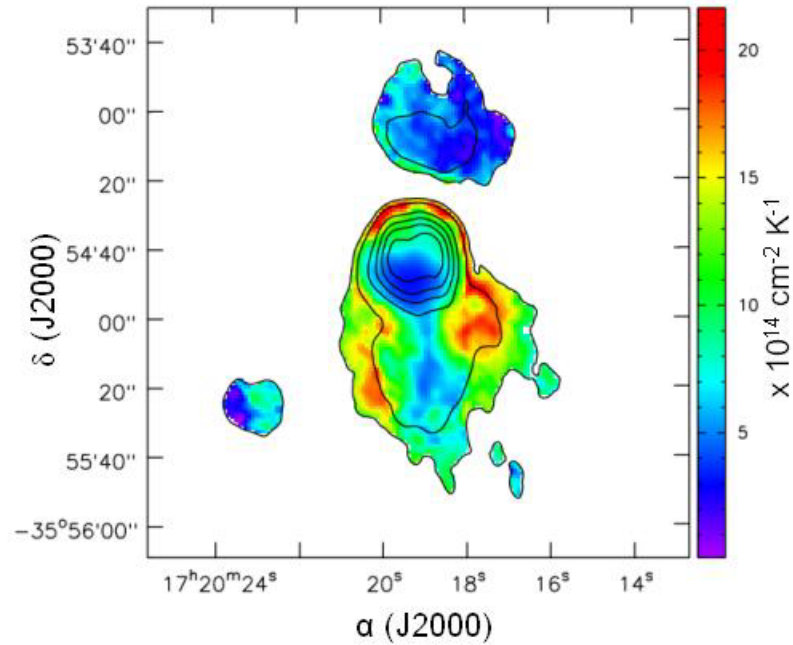


Fig. 3.5 -Plot of  $N(\text{OH})/T_{\text{ex}}$  toward source A in the NGC 6334 complex. The optical depths were integrated over the velocity range  $-6.3$  km/s to  $-1.3$  km/s. The contours represent the 1667 MHz continuum. Contour intervals are at 0.05, 0.1, 0.3, 0.5, 0.7, 0.9 of the peak continuum flux of 0.98 Jy/beam. The beam is  $8''.2 \times 5''.0$ .

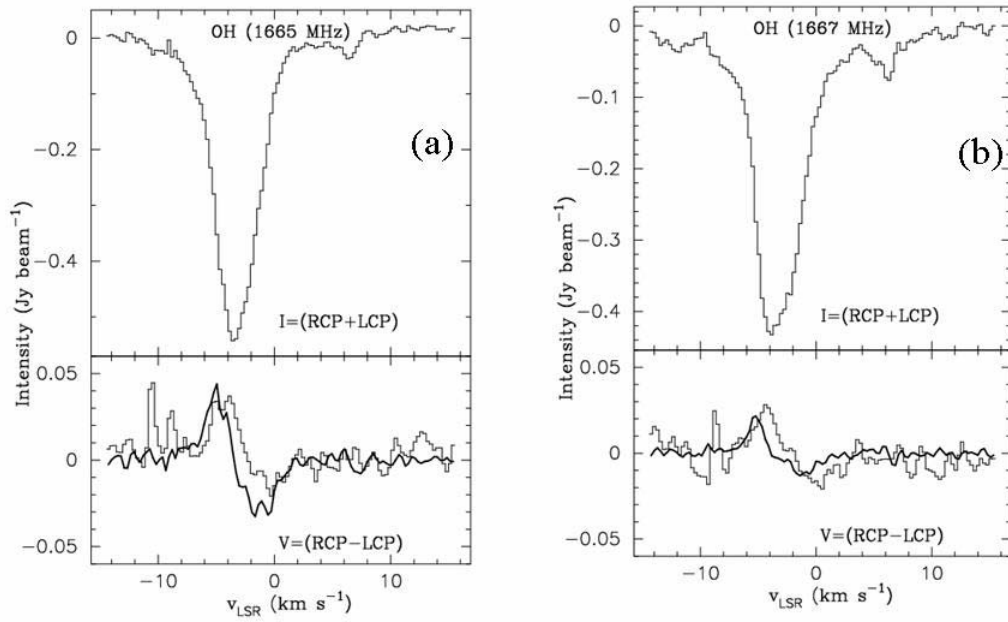


Fig. 3.6 -(a) Stokes I (*top*) and V (*bottom*) profiles in the OH 1665 MHz line toward Source A at the position  $\alpha=17^{\text{h}}16^{\text{m}}58^{\text{s}}.5$ ,  $\delta=-35^{\circ}51'35''$ . The continuous line superimposed on the V spectrum in the lower box is the derivative of  $I$  scaled by the derived value of  $B_{\text{los}}=595\pm 101\mu\text{G}$ . (b) Same as (a), but for OH 1667 MHz, and a derived value of  $B_{\text{los}}=536\pm 107\mu\text{G}$ .

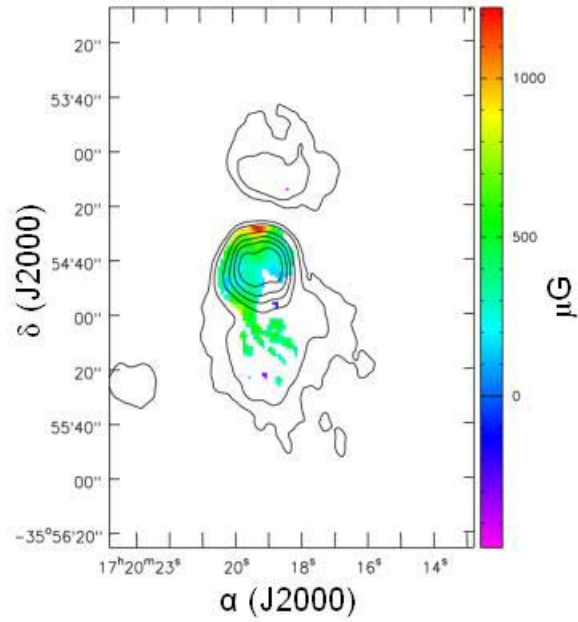


Fig. 3.7 -Map of magnetic field strengths toward source A overlaid with 1667 MHz continuum contours. Map shows the weighted average of field strengths in the OH 1665 and 1667 MHz mainlines. Contour intervals are at 0.05, 0.1, 0.3, 0.5, 0.7, 0.9 of the peak continuum flux of 0.98 Jy/beam. The beam is  $8''.2 \times 5''.0$ .

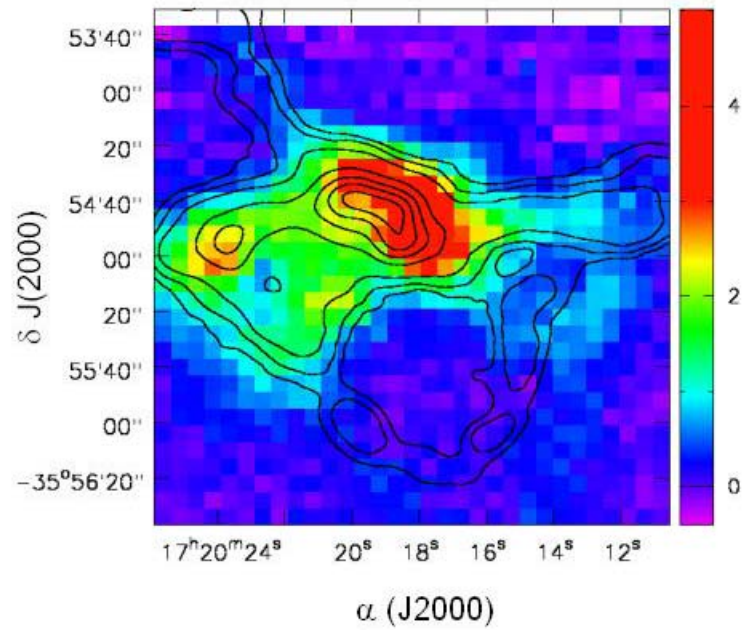


Fig. 3.8 -Integrated SiO line (colors) with 850  $\mu\text{m}$  contours at 0.9, 0.7, 0.5, 0.3, 0.1, 0.05, 0.025 x 15 Jy/beam

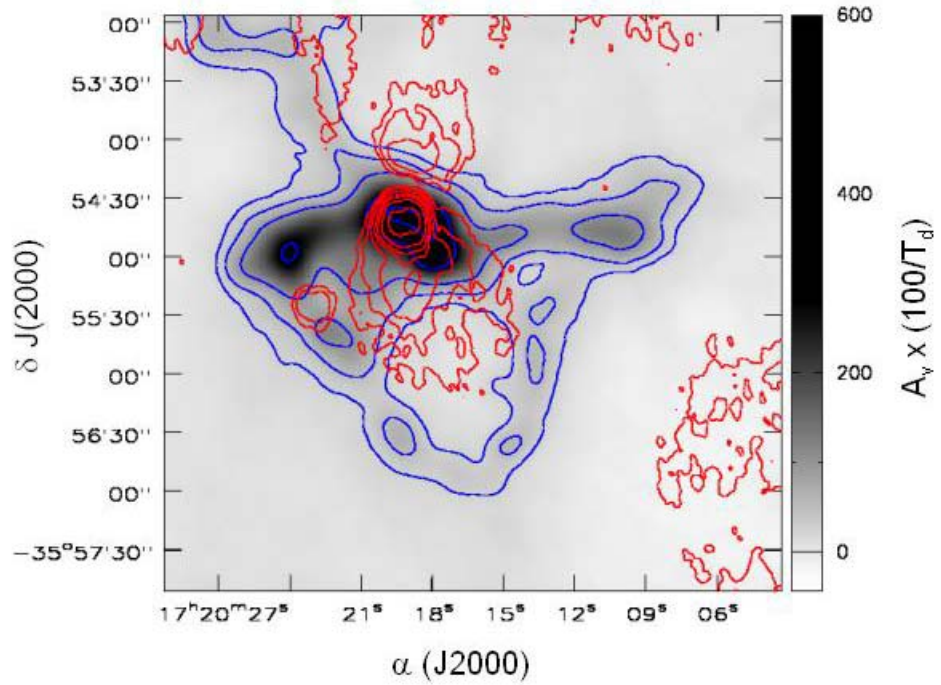


Fig. 3.9 - $850 \mu\text{m}$  dust emission (grey scale and blue contours) and  $1667 \text{ MHz}$  radio continuum emission (red contours). Blue  $850 \mu\text{m}$  contours represent  $A_v=500, 300, 100, 50$  and  $25 \times (100/T_d)$ , where  $T_d$  is the dust temperature.

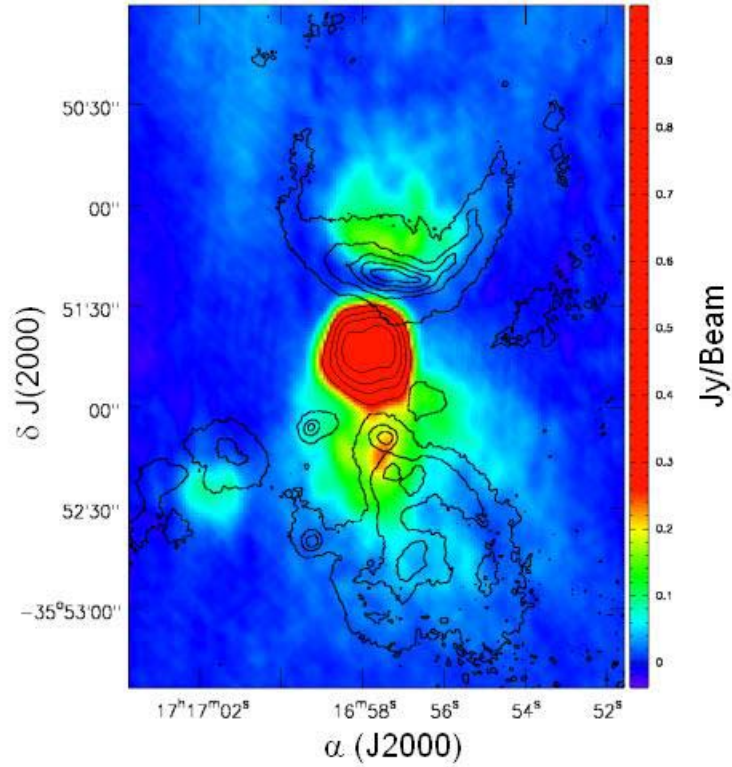


Fig. 3.10- 1667 MHz continuum (color and light contours at 0.9, 0.7, 0.5, 0.3  $\times$  0.98 Jy/beam) and 3.3  $\mu$ m PAH image (dark contours). Contours for 3.3  $\mu$ m at 0.9, 0.7, 0.5, 0.3, 0.1  $\times$  peak.

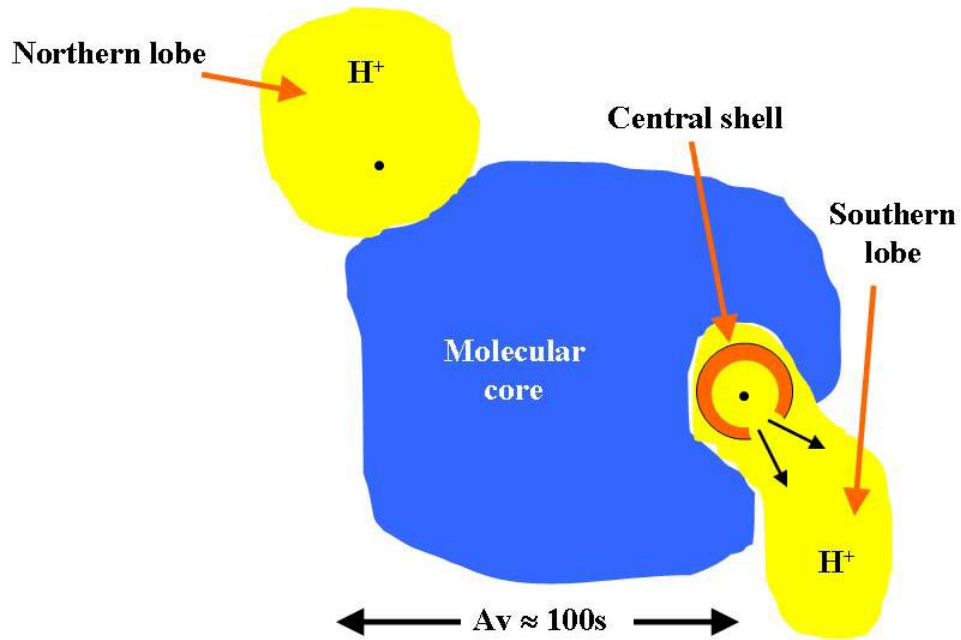


Fig 3.11 – Cartoon of NGC 6334 A region (observer is to the left). Ionized gas shown in yellow and red, molecular gas shown in blue. PDR (atomic) gas is not shown, it lies along ionized/molecular interfaces. Exciting stars are shown as small black dots.

# Chapter 4. VLA HI Zeeman Observations of the Cygnus X Region DR 22 and ON 2

## 1. Introduction

In this chapter we discuss Zeeman effect observations of 1420 MHz and 21 cm HI absorption lines toward radio continuum source DR 22 and ON 2 of the Cygnus X complex. In the remainder of §1 we review some details of the Cygnus X complex with a focus on DR 22 and ON 2; §2 details the observations and reduction of the data; §3 presents the results of our observations, §4 contains discussion of these results, and §5 conclusions drawn from our observations

### 1.1 The Cygnus X Star Forming Region

The Cygnus X region was first detected in 1952 by Piddington and Minnett as an extended, thermal radio source (Piddington and Minnett 1952). Since its discovery, the region has been surveyed at many different wavelengths, revealing many interesting objects including OB associations, young open clusters, compact HII regions and stellar nurseries. Structurally, the Cygnus X region is complex. Cygnus X lies along the galactic plane centered at a longitude of approximately  $80^\circ$ . The line of sight through this region lies along the spiral arm of the galaxy. In this direction, the region could be a “superposition of several complexes along the line of sight or a single coherent complex at a distance of 1.5 to 2 kpc” (Schneider et al. 2006). Kinematic distances to individual star-forming regions are difficult to determine. Despite this complexity, Cygnus X is geometrically favorable for Zeeman effect observations, due to the sensitivity of the Zeeman effect to the line-of-sight magnetic field. Based on starlight polarization studies, the magnetic field is known to be basically azimuthal to the plane of the Galaxy. This is the geometry that is expected if the field is coupled to the gas in a differentially rotating galaxy. Thus, Cygnus X is expected to lie along the mean field direction of the diffuse interstellar medium (ISM) of the galaxy.

We present 1420 MHz Zeeman observations of two compact HII regions within Cygnus X. Each source was selected based on their 1420 MHz



absorption profiles from the Canadian Galactic Plane Survey. The first is DR 22, an HII region first discovered by Downes and Rinehart in 1962. The second is ON 2, a region originally identified as an OH maser (Elder et al. 1969). Later observations of the ON 2 region showed the OH maser to be coincident with several ultra compact (UC)HII regions (Matthews et al 1973).

## **2. Observations and Data Reduction**

Observations were carried out by the VLA in the D configuration. Array parameters are detailed in table 4.1. Both circular polarizations of HI were observed simultaneously. A front-end transfer switch on each telescope was used to reverse the sense of circular polarization received at the telescope every 10 minutes in order to mitigate instrumental effects. This observing technique is described by Brogan and Troland (2001).

Editing, calibration, Fourier transformation, deconvolution, and processing of the HI data were carried out using the Astronomical Image Processing System (AIPS). Further data processing, including magnetic field calculations, were carried out in the Multichannel Image Reconstruction, Image Analysis and Display (MIRIAD) system.

## **3. Results**

### **3.1 Continuum**

#### **3.1.1 DR 22**

Figure 4.1 shows the 21 cm (1420 MHz) image of the discrete continuum source DR 22 and was made using the AIPS task IMAGR with a resolution of  $59'' \times 52''$ . There is only one independent resolution element across the source, thus these observations are sensitive to large-scale structure. Figure 4.1 shows DR 22 as having a central peak with a low intensity tail stretching eastward. At 50% of the peak continuum flux, the central region of DR 22 measures approximately  $1'$ . The tail extends to the east for  $7'.0$ .

#### **3.1.2 ON 2**

Figure 4.2 shows the 21 cm (1420 MHz) map of the discrete continuum sources of the ON 2 region. Figure 2 was made using the AIPS task IMAGR with

a resolution of 56''x53'' and one independent resolution element across each source. The continuum map shows two main discrete continuum sources: the northern HII source corresponding to G75.84+0.40 and the southern HII source corresponding to G75.77+0.34 (notation by Matthews and Spoelstra 1983, hereafter ON2 N and S respectively). There is also a weaker northern source that corresponds to G75.84+0.36 (hereafter ON2 NE). Low intensity continuum emission stretches between the ON2 N and ON2 S (Fig. 4.3). Finally an ultracompact (UC) HII region, G75.78+0.34, is associated with the strong OH maser for which the region was originally named. This source is unresolved in our continuum map.

### 3.2 HI Line Data

Optical depth profiles for the 1420 MHz HI line were calculated using the procedure outlined in Roberts et al. (1995). HI components were subject to severe saturation effects toward both DR 22 and ON2, with saturated channels having undefined optical depths. In order to mitigate this effect, we have used the procedure outlined in Brogan et al. (2001) to estimate the largest optical depth that can be reliably measured at each pixel given the continuum strength and  $\sigma$ . These limiting values then replaced those in the original optical depth cube that were either larger than the limiting value or undefined due to saturation effects. This procedure provided a lower limit for the optical depths in those channels affected by heavy saturation. Optical depth calculations were also masked at positions less than 7.5% and 2.5% of the maximum continuum brightness for DR22 and ON2 respectively.

#### 3.2.1 DR 22

The HI profiles consist of several blended velocity components and lie in the velocity range  $-15$  to  $+15$  km/s. There appear to be four different HI components with velocities of  $-7.0$ ,  $-0.5$ ,  $8.5$ , and  $14.0$  km/s. The component at  $-7.0$  km/s is not heavily saturated and therefore values were not replaced with a lower limit (see Fig. 4.4).

HI column density can be determined using the relation

$$N(\text{HI})/T_{\text{ex}} = 1.832 \times 10^{18} \int_{T_v} dv \text{ cm}^{-2} \text{ K}^{-1}.$$

Figures 4.5 and 4.6 show values for  $N(\text{HI})/\text{Tex}$  summed across the entire HI velocity range and the  $-7\text{km/s}$  component, respectively. In Figure 4.5, a morphological bias is introduced into the image that causes it to artificially resemble the continuum. This is due to large regions of the source being replaced at a given velocity and also where the continuum is weak. HI near  $-7\text{ km/s}$  is concentrated to the northwest of the continuum peak. A second peak in  $N(\text{HI})/\text{Tex}$  is evident in the central area of the continuum “tail” toward the east.

### **3.2.2 ON 2**

HI profiles toward ON 2 are also heavily saturated and thus replacement values were calculated for these regions. Applying the replacement technique described in §3.2 yields broad profiles toward ON 2 N and ON 2 S (Fig. 4.7). Both have center velocities of  $1.25\text{ km/s}$ . The weaker profile for ON 2 NE has a center velocity of  $3.8\text{ km/s}$ . Each profile has a FWHM of approximately  $15\text{ km/s}$ . Such broad profiles likely indicate that each single component actually consists of several blended components. The same morphological bias described above is introduced into any attempt to calculate HI column density toward ON 2.

## **3.3 Magnetic Fields**

To calculate the magnetic field strengths using the Zeeman effect, we fit a numerical derivative of the Stokes I spectrum to the Stokes V spectrum for each pixel in the data cubes with significant I and V signal. This process is described by Roberts et al. (1993). The results of this fit give the line-of-sight component of the magnetic field toward DR 22 and ON 2. By convention, a positive value of  $B_{\text{los}}$  indicates that the field is pointed away from the observer. We did not have significant magnetic field detections for the sources of ON 2. However, an upper limit of 3 times the 1-sigma error from the magnetic field fit can be placed on the magnetic field strengths of the ON 2 region. This yields a  $-45\text{ }\mu\text{G}$  3-sigma upper limit for ON 2 N and ON 2 S. Weak line strengths toward ON 2 NE limited the fitting process in this region.

### **3.3.1 DR 22**

We only considered the results to be significant if the derived value of  $B_{\text{los}}$  is greater than the  $3\sigma$  level. Under this condition, magnetic fields were detected

for DR 22 only. Average magnetic field strengths toward the core region of DR 22 were measured to be  $-84 \mu\text{G}$  at levels reaching  $9\sigma$ . The maximum magnetic field strength detected was measured to be  $181 \mu\text{G}$  at the  $3\sigma$  level to the east of the core in the low continuum brightness “tail” (§3.1.1). Figure 4.8 shows the Stokes I and V profiles toward the core region of DR 22 in 1420 MHz line of HI together with the derivative of the I profile scales with the fitted value of the magnetic field. Close examination of the profiles reveals that the line-of-sight magnetic field detection is associated with the velocity component at  $-7 \text{ km/s}$ . Negative values of  $B_{\text{los}}$  lie toward core region where HI gas is concentrated to the northwest of the continuum peak (fig. 4.6). A small region of significant positive  $B_{\text{los}}$  values lies toward the northern part of the low continuum brightness “tail”.

## 4. Discussion

### 4.1 ON 2

#### 4.1.1 Determination of the Central Ionizing Source from Radio Continuum Flux

Low frequency radio synthesis observations performed by Matthews and Spoeltra (1983) show two main structures in ON2 each containing the equivalent of one O star. These two structures are accompanied by a number of less bright components and an extended halo.  $J=1 \rightarrow 0$   $^{12}\text{CO}$  and  $^{13}\text{CO}$  transitions centered on ON 2 show evidence of small-scale complex structures associated with star-formation (Matthews et al. 1986). Radio continuum flux measurements provide an estimate for the type of star necessary to produce the ionizing field. The problematic quantity is the distance to the region. Purely kinematic estimates indicate a distance of 5.5 kpc, (Reifenstein et al. 1970). The possible association of ON 2 to the cluster Berkley 87 and related objects indicate a much closer distance of 900pc (Turner and Forbes 1982). Following the formulation described in Jackson and Kraemer (1999), we have estimated the required ionizing sources for ON2 N, S, and NE at both 5.5 and 1kpc based on the 1420 MHz radio continuum emission (table 4.2).

## 4.2 DR 22

### 4.2.1 Molecular Line Observations of the DR 22 Star-Forming Region

Schneider et al. 2006 performed a detailed study of the Cygnus X region of the  $^{13}\text{CO}$  2 $\rightarrow$ 1 and  $^{12}\text{CO}$  3 $\rightarrow$ 2 molecular lines. Low-J CO line surveys of nearby active star-forming regions probe molecular cloud clumps that contain the dense star-forming cores. The survey revealed that from  $v=-8$  to  $-2.8$  km/s the  $^{13}\text{CO}$  emission was dominated by a north-south elongated cloud connecting DR 22 and DR 23. At  $-4$  km/s this complex split into two separate clouds correlating with the DR 22 and DR 23 HII regions. The survey also revealed a cloud at a velocity of  $\sim+11$  km/s spatially coincident to the western part of DR 22 (Schneider et al. 2006).

### 4.2.2 Infrared Observations of the DR 22 Star-forming Region

Dutra and Bica (2001) performed a search for new infrared star clusters using the 2MASS atlas. They were able to identify one resolved star cluster in the region of DR 22, labeled as object 13 in table 1 of Dutra and Bica (2001). They also identified a related stellar group labeled object 14 surrounding object 13. Object 14 includes an infrared nebula positioned at  $\alpha(2000)=20\text{h}39\text{m}25.9\text{s}$ ,  $\delta(2000)=41^{\circ}20'02''$ . No candidate cluster was detected for this region due to a single bright point source centered on the nebula in the J-image.

LeDuigou and Knodleseder (2002) also used 2MASS observations to characterize new cluster candidates in the Cygnus X region. Cluster 11 (LeDuigou and Knodleseder 2002, table 3) can be identified with object 13 of Dutra and Bica (2001) and is coincident to the HII region DR22, with the center of DR 22 lying  $4'.6$  to the west. The cluster also lies  $2'.4$  from the center of IRAS 20375+4109. Assuming a distance of 1.5 kpc ( $DM=11$ ), LeDuigou and Knodleseder describe the cluster as globular, showing a dense core and powered by an O7 V central star.

Schneider et al. (2006) examined mid-infrared emission using MSX at 8.3 micron with a resolution of  $20''$ . The 8 micron emission traces UV heated small grains and PAHs in photon-dominated regions (PDRs). The images therefore

emphasize the interfaces between the molecular clouds and the UV fields of young, massive stars. Schneider et al. (2006) shows that the CO filament connecting DR 22 and DR 23 is associated with mid-IR emission tracing PDR interfaces due to early type stars close to the cloud. They believe most of the extended emission seen in the MSX images is due to PDR interfaces produced by CI 11 (LK2002) also known as object 14 (DB2001). The region also contains two MSX point-like sources embedded in the CO clumps of the DR22-DR23 filament. MSX6G80.9383-0.1268 also identified as IRAS20375+4109 is one of the brightest mid-IR sources in the region and is associated with clump 1 in table C.1 of Schneider et al. (2006).

#### **4.2.3 Radio Observations of the DR 22 Star-forming Region**

DR 22 is one of the sources observed during a survey of the Cygnus X region conducted by Downes and Rinehart (1966) at 5 GHz. Since the time of that survey, advances in technology have allowed high spatial resolution radio surveys to be conducted at several frequencies of the same region. Radio observations have produced some discrepancy as to the position of the DR 22 HII region. The Downes and Rinehart survey place DR 22 at  $\alpha(2000)=20^{\text{h}}39^{\text{m}}39.8^{\text{s}}$   $\delta(2000)=41^{\circ}14^{\text{m}}40.1^{\text{s}}$  while later surveys of individual sources such as Krassner et al. (1983) and Odenwald et al. (1986) place DR 22 at  $\alpha(2000)=20^{\text{h}}39^{\text{m}}25.8^{\text{s}}$   $\delta(2000)=41^{\circ}19^{\text{m}}54.3^{\text{s}}$ . This discrepancy is resolved by Wendker (1991) whose observations at 1.4 GHz show DR 22 to have a total extent of 20' and a complex morphology. The arcsecond resolution maps of Krassner et al. (1983) and Odenwald et al. (1986) show only the 20" core of the bright northwestern component.

The observations detailed in this study correspond to the same bright, northwestern component of DR 22 as detailed by Krassner et al. (1983) and Odenwald et al. (1986). Comparing the infrared studies described above with the continuum morphology discussed in §2.1, we find that the position of this component corresponds spatially to that of the near-IR nebula reported by Dutra and Bica (2001) from 2MASS observations and also the mid-Infrared source MSX6G80.9383-0.1268 also identified as IRAS20375+4109 (Fig. 4.9).

Assuming the region is powered by a single star, several estimates of the spectral type of the early-type star necessary to produce the observed UV field have been made for the north-western component described above. Based on Far-IR and radio emission measurements, Odenwald et al. (1986) determined an O6 ZAMS star would be necessary to produce the observed field. Krassner et al. (1983) determined, based on 2.7 GHz observations, that the excitation required one O8 ZAMS star. Also, as described in §3.1 LeDuigou and Knodlseder (2002) determined that the central star powering CI 11 in the DR 22 region must be an O7 ZAMS star.

Based on the radio flux of the 1420 MHz continuum map, we have determined that the spectral class of a single early type star necessary to produce the observed UV field is either an O8 or O8.5 ZAMS star. For the purpose of this calculation we have adopted a distance of 2 kpc. This correlates with Schneider et al. (2006) who believe the objects in Cygnus X are at approximately the same distance of 1.7 kpc and Odenwald et al. (1993) who places DR 22 in with a group objects located at 2 kpc.

#### **4.2.4 Calculation of Total Hydrogen Column Density for the DR 22 Core Region**

We estimate the total column density of N(H) from J, H, and  $K_s$  2MASS data for the point source detected at the center of the infrared nebula that corresponds to our HII region. Assuming an O8 to O8.5 ZAMS star as the central ionizing source at a distance of 2 kpc we predict the apparent visual magnitude of the central star without extinction to be 7.0 applying table 5 of Vacca et al. (1996). Based on Koorneef (1983) table 3 we calculate  $m_J=7.7$ , yielding  $A_J=4.8$  and  $\tau_J=4.4$ . Applying  $N(H)=\tau/c_\lambda$  with the grain optical depth per hydrogen atom,  $c_\lambda$  determined from Cloudy modeling of the interstellar medium (Ferland et al. 1998), we find the total hydrogen column density to be  $3.4 \times 10^{22} \text{ cm}^{-2}$ . This corresponds to a large visual extinction ( $A_V=18$  mags) in the direction of DR 22, which would effectively obscure the ionizing star. This column density is also in good agreement with the molecular hydrogen column density determined from  $^{13}\text{CO}$  observations by Schneider et al. (2006). They report

$N(\text{H}_2)=3.02 \times 10^{22} \text{ cm}^{-2}$  for DR 22 clump 1 in table C.1 (Schneider et al. 2006). Clump 1 corresponds spatially to our HII region.

#### 4.2.5 Magnetic Support and Virial Estimates for the DR 22 Core Region

A principal goal of this study is to determine the effect of the magnetic field on the dynamics and evolution of the DR 22 star-forming region. Such estimates require that certain physical parameters of the region be known including  $\text{H}_2$  column density, internal velocity dispersion, radius, and total mass. We apply the concepts outlined in Crutcher (1999) to analyze the magnetic effects on DR 22.

We have detailed the calculation of the  $\text{H}_2$  column density in §4.2.4. We adopt the value of the mass determined by Schneider et al (2006) from  $^{13}\text{CO}$  observations,  $M=4200M_{\text{sun}}$ . The radius of the molecular cloud is calculated as that which reproduces the mass determined from Schneider et al. (2006),  $r=1.3\text{pc}$ . We estimate the internal velocity dispersion  $\sigma$ , to be 1.06 km/s. This is derived from line widths of optically thin  $\text{H}_2\text{CO}$  observations of Piepenbrink and Wendker (1988) and  $^{13}\text{CO}$  observations of Schneider et al. (2006). We adopt a  $T_k=15\text{K}$  based on the  $^{13}\text{CO}$  studies of Schneider et al. (2006). Table 4.3 lists the derived parameters for DR 22.

The relation  $B_{s,\text{crit}}=5 \times 10^{-21} N_p \mu\text{G}$  provides an estimate of the static magnetic field in the cloud that would completely support it against gravity. If the actual field in the cloud is comparable to  $B_{s,\text{crit}}$ , it can be judged to be dynamically important to the region. For DR 22 we find  $B_{s,\text{crit}}=340 \mu\text{G}$ . Following Crutcher (1999) we apply the following statistical correction to calculate the total magnetic field strength:  $B=2*B_{\text{los}}$  and  $B^2=3*B_{\text{los}}^2$ . This yields a total estimated magnetic field strength of 168  $\mu\text{G}$ , approximately half of the field strength necessary to completely support the cloud against gravity. The mass-to-magnetic flux ratio is 2.0, also indicating that the cloud is magnetically supercritical.

The parameter  $\beta_p$  is the ratio of thermal to magnetic pressure where  $\beta_p=2(m_A/m_s)^2$ :  $m_A$  is the magnetic Mach number and  $m_s$  is the turbulent mach number (see chapter 3, §4.1). Our data shows  $\beta_p \approx 0.01$ .  $\beta_p < 1$  indicates that the magnetic pressure dominates thermal pressure. Virial estimates for this cloud show  $\mathcal{F} \approx \mathcal{M}$ , or that the kinetic and magnetic energy densities are in approximate



equilibrium. This is expected if the magnitude of the fluctuating part of the magnetic field is equal to the magnitude of the static field (Crutcher 1999). In terms of virial equilibrium,  $2\mathcal{T} + \mathcal{M} \approx 0.6\mathcal{W}$ . This does not include the external pressure term, which acts in the same sense as the gravitational term, indicating the cloud is in approximate virial equilibrium. Table 4.4 lists parameters of magnetic significance and virial estimates based on the analysis above.

Table 4.1  
OBSERVATIONAL PARAMETERS FOR VLA OBSERVATIONS

Parameter	HI
Date.....	May 2 <sup>nd</sup> , 2003 and May 5 <sup>th</sup> , 2003
Configuration.....	D
R.A. of field center (J2000).....	20 <sup>h</sup> 39 <sup>m</sup> 26 <sup>s</sup>
Decl. of field center (J2000).....	41°20'00.0"
Total Bandwidth (MHz).....	0.78
Number of Channels.....	256
Hanning smoothing.....	No
Channel Spacing (km/s).....	0.64
Approximate time on source (hr)	
DR 22.....	6
ON 2.....	6
Rest Frequency (MHz).....	1420.406
FWHM of synthesized beam.....	
DR 22.....	59"x52"
ON 2.....	56"x53"
RMS noise (mJy/beam).....	
Line channels	
DR 22.....	13
ON 2.....	8
Continuum	
DR 22.....	14
ON 2.....	9

TABLE 4.2  
DERIVED EXCITING STARS FOR ON 2 REGION

SOURCE	POSITION		Radio Flux	EXCITING STAR	
	R.A. (J2000)	Decl. (J2000)		1 kpc	5.5 kpc
ON 2 N	20 21 38.0	37 31 13	4.03	B0	06
ON 2 S	20 21 41.6	37 30 53	3.09	B0	06-06.5
ON 2 NE	20 21 49.7	37 30 13	0.15	B0.5	B0

NOTE. ---Units of right ascension are hours, minutes, and seconds, and units of declination are degrees, arcminutes, and arcseconds. Radio flux is in Jy.

TABLE 4.3  
DR 22 PARAMETERS

Parameter	Value
Radius (r).....	1.3 pc
Mass (M).....	4200 $M_{\text{sun}}$
N(H).....	$3.4 \times 10^{22} \text{ cm}^{-2}$
$n_p$ .....	$1.5 \times 10^4 \text{ cm}^{-3}$
$T_k$ .....	15K
$\Delta u$ .....	2.5 km/s
$B_{\text{los}}$ .....	84 $\mu\text{G}$

TABLE 4.4  
DR22: DERIVED VALUES AND  
VIRIAL ESTIMATES

Parameter	Value
$m_A$ .....	0.60
$m_S$ .....	8.0
$\beta_p$ .....	0.01
$[M/\Phi_B]_{\text{obs/crit}}$ .....	2.0
$\mathcal{W}$ .....	$7.8 \times 10^{47}$ ergs
$\mathcal{T}$ .....	0.18
$\mathcal{M}$ .....	0.22

NOTE.--- $m_A$  is the magnetic Mach number,  $m_S$  is the turbulent Mach number,  $M/\Phi_B$  is the mass to magnetic flux ratio,  $\mathcal{W}$  is the virial gravitational energy,  $\mathcal{T}$  is the virial kinetic energy, and  $\mathcal{M}$  is the virial magnetic energy; all terms are defined in Crutcher (1999).

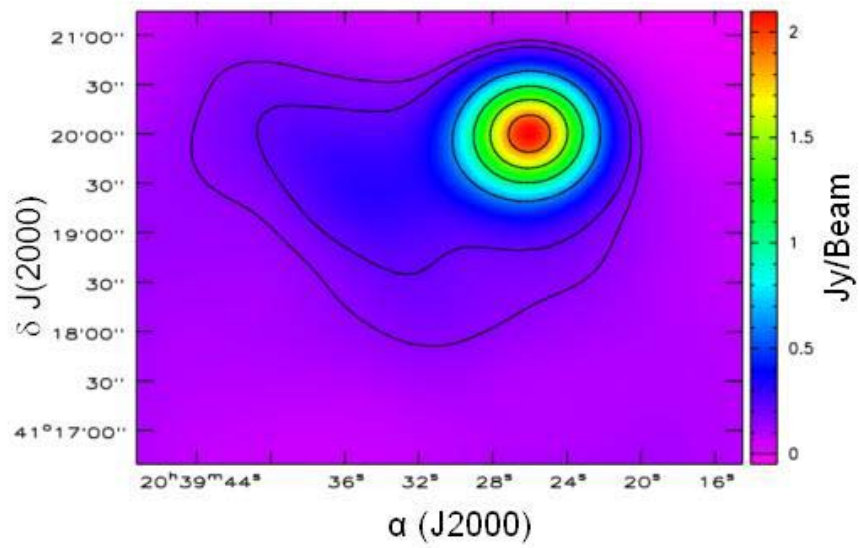


Fig. 4.1 -21cm continuum map of DR 22 at 1420 MHz. Contour intervals are at 0.075, 0.1, 0.3, 0.5, 0.7, 0.9 of the peak continuum flux of 2.1 Jy/beam. The beam is  $59'' \times 52''$ .

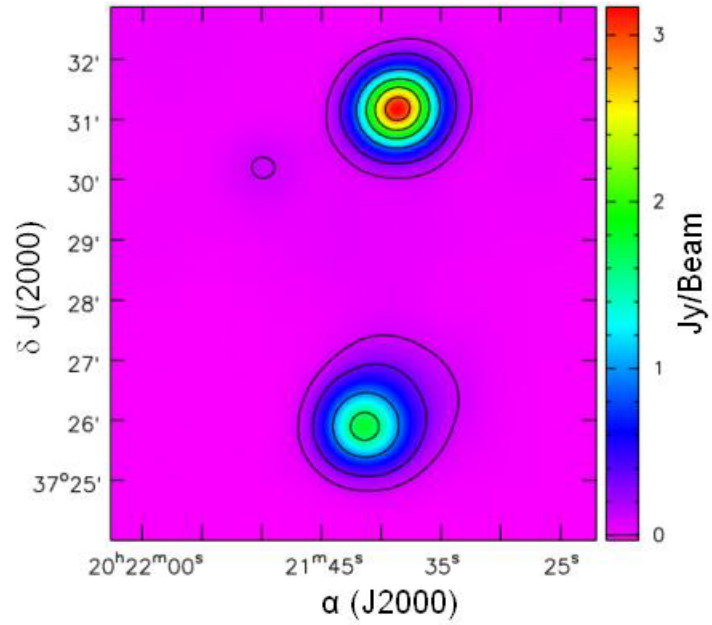


Fig. 4.2 -21cm continuum map of ON 2 at 1420 MHz. Contour intervals are at 0.03, 0.1, 0.3, 0.5, 0.7, 0.9 of the peak continuum flux of 3.1 Jy/beam. The beam is 56"x53".

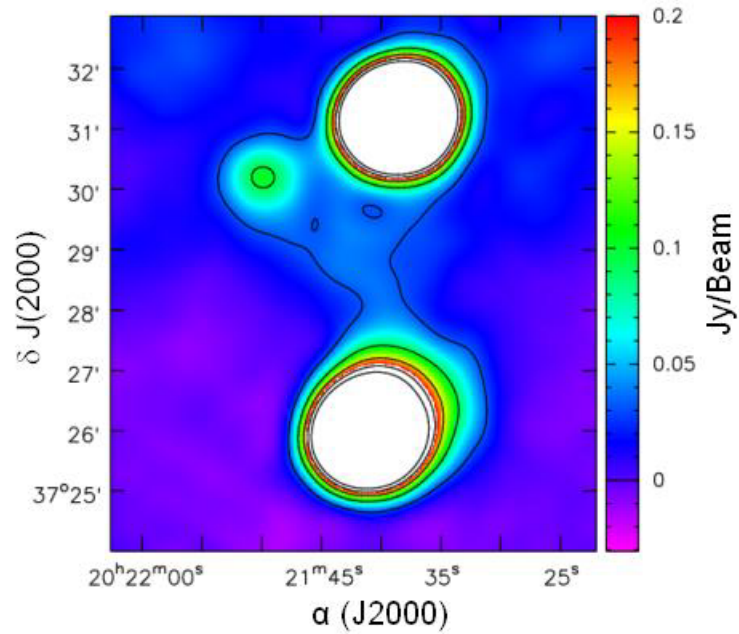


Fig. 4.3 -21cm continuum map of ON 2 at 1420 MHz. Contour intervals are at 0.01, 0.03, 0.05, 0.07, 0.09 of the peak continuum flux 3.1 Jy/beam. The beam is 56"x53".



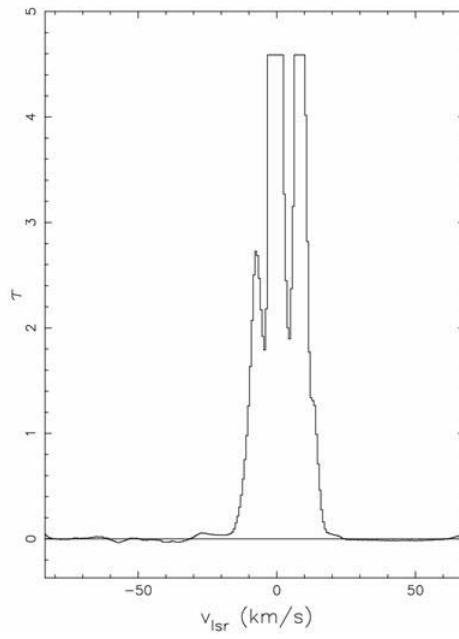


Fig. 4.4 -HI 1420 MHz optical depth profile toward the core of DR 22 at  $\alpha=20^{\text{h}}39^{\text{m}}26^{\text{s}}.5$ ,  $\delta=41^{\circ}20'01''$ .

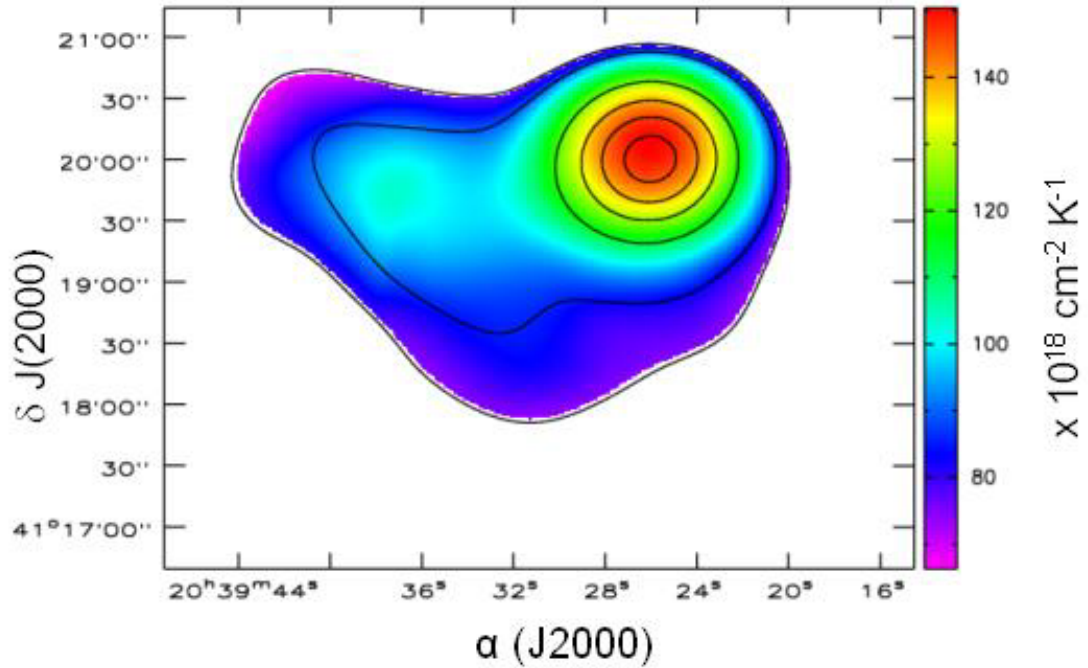


Fig. 4.5 -Plot of  $N(\text{HI})/T_{\text{ex}}$  toward DR 22. The optical depths were integrated over the velocity range  $-30.8$  km/s to  $26.6$  km/s. The contours represent the 1420 MHz continuum. Contour intervals are at 0.075, 0.1, 0.3, 0.5, 0.7, 0.9 of the peak continuum flux of 2.1 Jy/beam. The beam is  $59'' \times 52''$ .

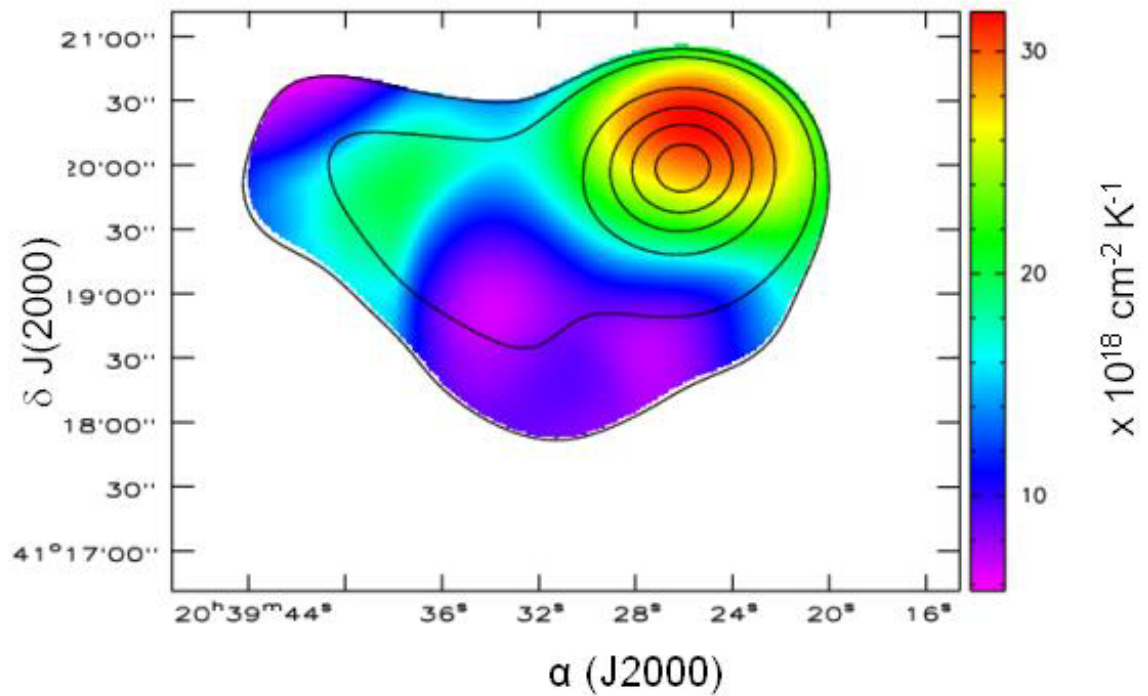


Fig. 4.6 -Plot of  $N(\text{HI})/\text{Tex}$  toward DR 22. The optical depths were integrated over the velocity range  $-19.8$  km/s to  $-5.0$  km/s. The contours represent the 1420 MHz continuum. Contour intervals are at 0.075, 0.1, 0.3, 0.5, 0.7, 0.9 of the peak continuum flux of 2.1 Jy/beam. The beam is  $59'' \times 52''$ .

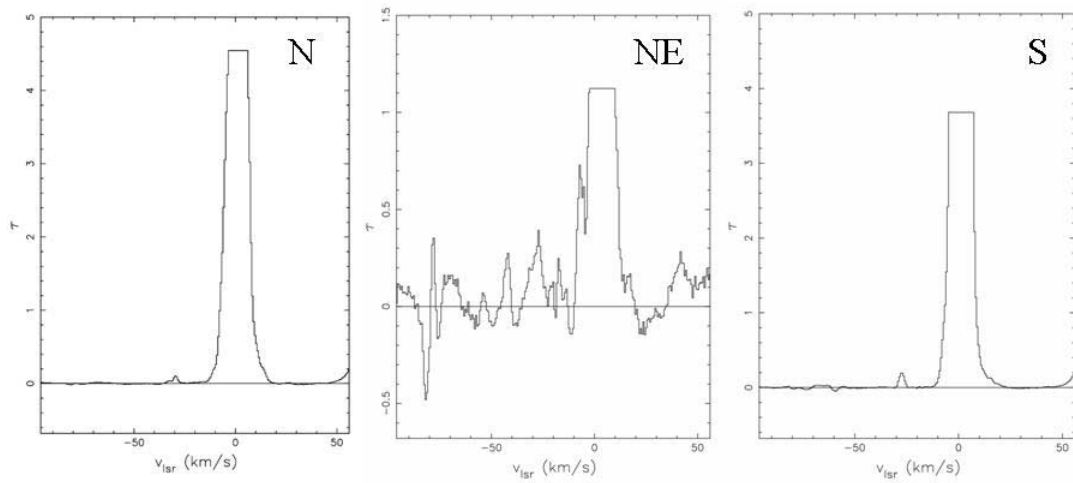


Fig. 4.7 -HI 1420 MHz optical depth profile toward (a) ON 2N  $\alpha=20^{\text{h}}21^{\text{m}}38^{\text{s}}.3$ ,  $\delta=37^{\circ}31'08''$ ; (b) ON 2NE at  $\alpha=20^{\text{h}}21^{\text{m}}49^{\text{s}}.7$ ,  $\delta=37^{\circ}30'08''$ ; (c) ON 2S  $\alpha=20^{\text{h}}21^{\text{m}}40^{\text{s}}.3$ ,  $\delta=37^{\circ}26'12''$ .

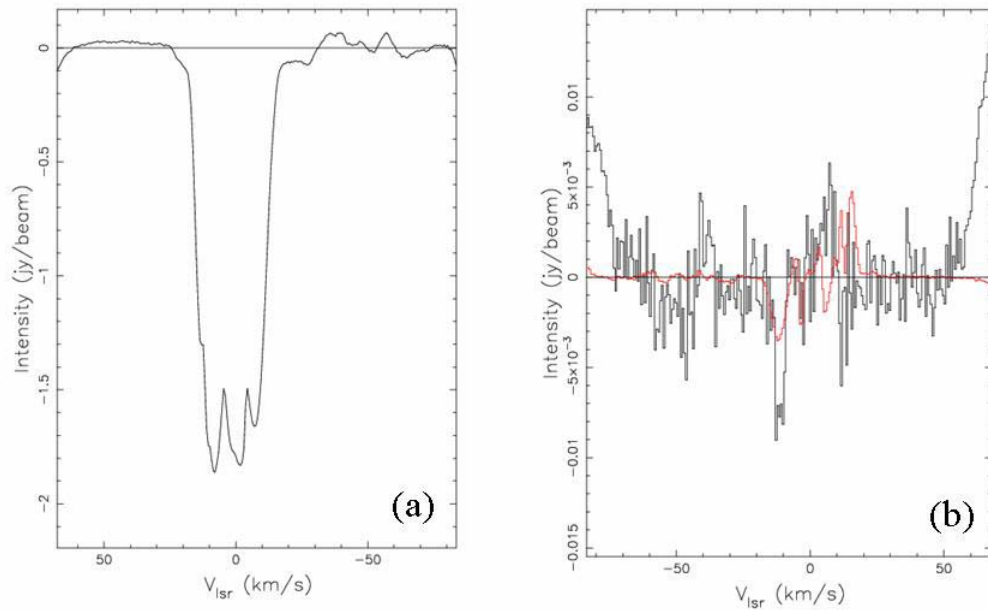


Fig. 4.8 -(a) Stokes I (*left*) and (b)V (*right*) profiles in the HI 1420 MHz line toward DR 22 at the position  $\alpha=20\text{h}39\text{m}24\text{s}.8$  ,  $\delta=41^{\circ}20'08''$ . The red line superimposed on the V spectrum is the derivative of I scaled by the derived value of  $B_{\text{los}}=-84\pm 11\mu\text{G}$ .

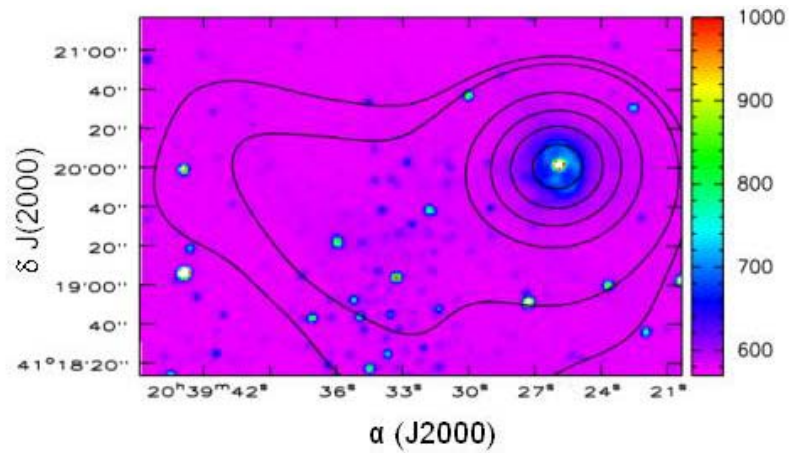


Fig. 4.9 -K Band image of DR 22 from 2MASS. The contours represent the 1420 MHz continuum. Contour intervals are at 0.075, 0.1, 0.3, 0.5, 0.7, 0.9 of the peak continuum flux of 2.1 Jy/beam. The beam is 59"x52".

## Chapter 5. Summary and Conclusions

### 1. Summary of Results

#### 1.1 NGC 6334 A

High resolution 1665 MHz and 1667 MHz OH Zeeman observations of the NGC 6334 A region allow for a better analysis of spatial variations of the magnetic field. We have also extended this study to include a comprehensive model of the region based on our own OH opacity studies as well as multi-wavelength observations of the region.

##### 1.1.1 A New Model

Based on OH opacity studies, dust continuum maps, radio spectral lines, and IR maps we have developed a new model for the NGC 6334 A region. This model consists of a massive, elongated molecular core embedded within a lower density molecular envelope of comparable mass and five times larger dimensions. Within the core, at least one O7.5 ZAMS star has formed and created a shell-like ultra-compact HII (UCHII) region. The ionized gas shell is now nearly as large in diameter as the molecular core and is beginning to break out of an opening on the back side of the molecular core creating a champagne flow to the south. Thus, the UCHII region lies behind most of the molecular core, hidden by several hundred magnitudes of visual extinction. Also, an independent HII region has formed north of the molecular core where the extinction is relatively low. This HII region is excited by a later type star that appears as IRS 54. The northern lobe appears superficially to be the northern extension of a biconical HII region. But this appearance is only an illusion.

##### 1.1.2 Magnetic Effects

Toward NGC 6334 A, line-of-site magnetic field strengths were determined to be 600  $\mu\text{G}$  based on OH Zeeman effect measurements. This gives a mass-to-flux ratio ( $M/\Phi$ ) equal to 5 indicating that magnetic energy is smaller than gravitational energy in the core. This suggests that the core is magnetically supercritical and the magnetic field strength is not enough to support the core against gravitational collapse. We also find internal motions within the molecular

to be highly supersonic and thermal energy to be insignificant compared to turbulent energy. Finally, the magnetic energy density is found to be comparable to the turbulent energy density, a situation called magnetic equipartition. This is expected when the turbulent motions in the cloud are caused by transverse Alfvén waves rather than true turbulence.

## **1.2 Cygnus X**

We have observed HI absorption toward DR 22 and ON2 in the Cygnus X region with the VLA. We have only one independent resolution element across each source. The HI profiles for each source are severely saturated with several blended components.

### **1.2.1 ON 2**

HI Zeeman observations toward ON 2 failed to detect line-of-sight magnetic fields. However, based on 1420 MHz radio continuum flux observation, the stars necessary to produce the ionizing fields of each of the three resolved sources can be computed. These estimates are recorded in table 4.2. We provide estimates based on distances of both 5.5 kpc and 1 kpc due to the lack of agreement in the literature of the distance to ON 2.

### **1.2.2 DR 22**

We have calculated  $N(\text{HI})/T_{\text{ex}}$  summed across the  $-7\text{km/s}$  component of DR 22.  $N(\text{HI})/T_{\text{ex}}$  increases to the northwest of the continuum peak and toward the central regions of the low continuum brightness “tail”.

We find the HII region of our 1420 MHz continuum observations to be spatially associated with the near-IR nebula reported by Dutra and Bica (2001) from 2MASS observations and also the mid-Infrared source MSX6G80.9383-0.1268 also identified as IRAS20375+4109 (Fig. 4.9). The observed HII region is also associated with clump 1 of the  $^{13}\text{CO}$  observations of Schneider et al. (2006).

Magnetic fields were only detected toward DR 22 associated with the  $-7\text{km/s}$  velocity component.  $B_{\text{los}}$  toward the core region of DR22 is of the order  $-84\mu\text{G}$  and  $+180\mu\text{G}$  toward the north central region of the “tail”. Observed and derived parameters indicate the DR 22 core region to be magnetically supercritical and in approximate virial equilibrium. Virial estimates also show the



kinetic and magnetic energies to be approximately equal indicating the magnitude of the static magnetic field is approximately equal to the magnitude of the fluctuating part of the magnetic field.

## 2. Magnetic Fields in Molecular Clouds

### 2.1 Comparison to Crutcher (1999)

Crutcher (1999) provided a summary of 27 sensitive Zeeman measurements of magnetic fields in molecular clouds. Only 15 clouds presented showed magnetic field detections. Together with observational and derived parameters, the relative importance of the gravitational, kinetic, and magnetic energies in dense clouds was assessed. The results for NGC 6334 A and DR 22 can be compared with the conclusions presented for the statistical study of the 15 clouds with magnetic field detections. Table 5.1 lists the values for the parameters  $m_S$ ,  $m_A$ ,  $\beta_\rho$ , and  $M/\Phi_B$  (described in chapter 3 §4.2 and chapter 4 §4.2.5) for the ensemble of 15 clouds presented in Crutcher (1999), and, also for NGC 6334 A and DR 22.

Crutcher (1999) showed that velocity dispersions in his sample of self-gravitating clouds are supersonic and approximately equal to the Alfvén velocity. This circumstance suggests that macroscopic motions in these clouds are due to MHD waves. In agreement with this conclusion, both NGC 6334 A and DR 22 exhibit approximate magnetic equipartition, suggesting that turbulent motions in these clouds, too, are caused by transverse Alfvén waves.

Mass-to-flux ratios for NGC 6334 A and DR 22 are 5 and 2, respectively, (after application of the same statistical correction factor of 2 used by Crutcher, that is,  $B_{\text{tot}} \approx 2 B_{\text{los}}$ ). Therefore, the NGC 6334 A and DR 22 clouds appear to be magnetically supercritical, assuming that the total field strengths  $B_{\text{tot}}$  in these regions do not greatly exceed the measured values of  $B_{\text{los}}$ . Crutcher (1999) found the mass-to-flux ratio for the 15 clouds with magnetic field detections to be 2 with no direct observational evidence for magnetically subcritical clouds.

Also in agreement with Crutcher (1999), the analysis of DR 22 shows that magnetic effects dominate thermal effects and that the kinetic and magnetic energies are approximately the same ( $\mathcal{T} \approx \mathcal{M}$ , table 4.4). Also, a comparison of

magnetic and kinetic energies to the gravitational energy shows both DR 22 and NGC 6334 A to be in approximate virial equilibrium (see chapter 3 §4.1 and chapter 4 §4.2.5). Note that the mass estimate provided for NGC 6334 A assumes virial equilibrium; however, a similar total mass is estimated from the 850  $\mu\text{m}$  dust continuum map.

Finally, we consider the quantity  $\kappa$  which parameterizes the relationship between the gas density and the magnetic field strength, usually stated as a power law,  $|B| \propto \rho^{\kappa}$  (Crutcher 1999). If the magnetic field is unimportant throughout the collapse of a spherical cloud, then the conservation of mass and flux predicts  $\kappa=2/3$ . If the magnetic field is important, theoretical formulations predict a smaller value of  $\kappa$ , typically close to 1/2. For example, numerical modeling of ambipolar diffusion driven cloud contraction yields  $\kappa \approx 0.47$  (Fiedler & Mouschovias 1993). Thus, measurements of magnetic field strength and gas density can test the theoretical models of cloud contraction as described in chapter 1 §3.3. Figure 1 in Crutcher (1999) is a plot of  $\log B_{\text{los}}$  vs.  $\log n(\text{H}_2)$ . Through linear regression techniques based on the magnetic field and gas density measurements, Crutcher (1999) determined  $\kappa=0.47 \pm 0.08$ , consistent with the prediction of ambipolar diffusion driven cloud evolution. Including the results of the above analysis for NGC 6334 A and DR 22 as data points (tables 3.2 and 4.3) on this same plot shows these clouds follow the trend presented by Crutcher (1999). Therefore, results for these two clouds are also consistent with the ambipolar diffusion model. However, Crutcher (1999) also points out that this result could also be implied by  $m_A$  being invariant from cloud to cloud. The origin of an invariant  $m_A$  is not clearly understood, such a phenomenon need not necessarily be related to ambipolar diffusion.

## 2.2 Conclusions

In agreement with the results of the analysis of Crutcher (1999) our data show that static magnetic fields are important in the support of cores against gravity. However, Alfvénic motions are also present and provide turbulent support to the cores with energies comparable to magnetic energies. Finally a comparison of our detected magnetic field strengths and gas densities to the plot

presented in Crutcher (1999) indicates that cloud collapse in NGC 6334 A and DR 22 is ambipolar diffusion driven. The analysis of the cloud cores NGC 6334 A and DR 22 further confirms that the magnetic field plays a crucial role in the physics governing the dynamics and evolution of star formation.

Table 5.1  
MAGNETICALLY SIGNIFICANT PARAMETERS

Parameter	Ensemble of 27 Clouds Crutcher (1999)	NGC 6334 A	DR 22
$m_A$ .....	1.0	0.6	0.6
$m_S$ .....	5.0	4.0	8.0
$\beta_\rho$ .....	0.04	0.04	0.01
$[M/\Phi_B]_{\text{obs/crit}}$ .....	2.0	5.0	2.0

NOTE.--- $m_A$  is the magnetic Mach number,  $m_S$  is the turbulent Mach number, and  $M/\Phi_B$  is the mass to magnetic flux ratio; all terms are defined in Crutcher (1999). As in Crutcher (1999), we have applied a statistical correction factor of 2 in order to estimate total magnetic field from the observed field, that is, we assume  $B_{\text{tot}} \approx 2 B_{\text{los}}$ .

## References

- Abel, N.P., Brogan, C.L., Ferland, G.J., O'Dell, C.R., Shaw, G., & Troland, T. H. 2004, ApJ, 609, 247
- AIPS Cookbook , <http://www.aips.nrao.edu/CookHTML/CookBook.html>
- González-Avilés, M., Lizano, S., & Raga, A.C. 2005, ApJ, 621, 359
- Breitschwerdt, D., & Drury, L. O'C. 1991, A&A, 245, 257
- Brogan, C.L., & Troland, T.H. 2001, ApJ, 560, 821
- Brogan, C.L., & Troland, T.H. 2001, ApJ, 550, 799
- Brooks, K.J., & Whiteoak, J.B. 2001, Mon. Nor. R. Astron. Soc., 320, 465
- Burton, M.G., Ashley, M.C.B., Marks, R.D., Schinckel, A E., Storey, J.W.V., Fowler, A., Merrill, M., Sharp, N., Gatley, I., Harper, D.A., Loewenstein, R.F., Mrozek, F., Jackson, J.M., & Kraemer, K.E. 2000, ApJ, 542, 359
- Campbell, M.F., Hoffman, W.F., Thronson, H.A., Jr., Niles, D., Nawfel, R., & Hawrylycz, M. 1982, ApJ, 261, 550
- Carral, P., Kurtz, S.E., Rodríguez, L.F., Menten, K., Cantó, J., & Arceo, R. 2002, AJ, 123, 2574
- Comerón, F., & Torra, J. 2001, A&A, 375, 539
- Crutcher, R.M. 1977, ApJ, 216, 308
- Crutcher, R.M. 1999, ApJ, 520, 706
- Crutcher, R., Heiles, C., & Troland, T. 2003, LNP, 614, 155
- Crutcher, R.M., Troland, T.H., Goodman, A.A., Heiles, C., Kazes, I., & Myers, P.C. 1993, ApJ, 407, 175
- Davis, L., Jr., & Greenstein, J.L. 1951, ApJ, 114, 206
- Dent, W.R.F., Macdonald, G.H., & Andersson, M. 1988, Mon. Not. R. Astr. Soc., 235, 1397
- dePree, C.G., Rodriguez, L.F., Dickel, H.R., & Goss, W.M. 1995, ApJ, 447, 220

Dickel, H.R., Dickel, J.R., & Wilson, W.J. 1977, ApJ, 217, 56

Downes, D., & Rinehart, R. 1966, ApJ, 144, 937

Dutra, C.M., & Bica, E. 2001, A&A, 376, 434

Elitzur, M. 1992, *Astronomical Masers*, (Dordrecht: Kluwer)

Eldér, J., Rönnäng, B., & Winnberg, A. 1969, Natur., 222, 67

Ferland, G.J., Korista, K.T., Verner, D. A., Ferguson, J.W., Kingdon, J.B., & Verner, E.M. 1998, PASP, 110, 761

Fiedler, R.A., & Mouschovias, T. Ch. 1993, ApJ, 415, 680

Forster, J.R., Whiteoak, J.B., Gardner, F.F., Peters, W.L., & Kuiper, T.B.H. 1987, PASAu, 7, 189

Hall, J.S. 1949, Sci, 109, 166

Harvey, P.M., & Gatley, I. 1983, ApJ, 269, 613

Harvey, P.M., Hyland, A.R., & Straw, S.M. 1987, ApJ, 317, 173

Heiles, C. 2000a, AJ, 119, 923

Hiltner, W.A. 1949, ApJ, 109, 471

Hoare, M.G. Roche, P.F., & Glencross, W.M. 1991, MNRAS, 251, 584

Jackson, J.M., & Kraemer, K.E. 1999, ApJ, 512, 260

Kassis, M., Adams, J.D., Campbell, M.F., Deutsch, L.K., Hora, J.L., Jackson, J.M., & Tollestrup, E.V. 2006, ApJ, 637, 823

Koornneef, J. 1983, A&A, 128, 84

Kraemer, K.E., Jackson, J.M., Paglione, T.A.D., & Bolatio, A.D. 1997, ApJ, 478, 614

Kraemer, K.E., Deutsch, L.K., Jackson, J.M., Hora, J.L., Fazio, G.G., Hoffman, W.F., & Dayal, A. 1999, ApJ, 516, 817

Kraemer, K.E. & Jackson, J.M. 1999, ApJ, 124, 439

Kraemer, K.E., Jackson, J.M., Lane, A.P., & Paglione, T.A.D. 2000, ApJ, 542, 946

Krassner, J., Pipher, J.L., Savedoff, M.P., Soifer, B.T. 1983, AJ, 88, 972

Landecker, T.L. 1984, AJ, 89, 85L

Le Duigou, J.M., & Knödseder, J. 2002, A&A, 392, 869

MacLaren, I., Richardson, K.M., & Wolfendale, A.W. 1988, ApJ, 333, 821

Matthews, H.E., Goss, W.M., Winnberg, A., & Habing, H.J. 1973, A&A, 29, 309

Matthews, H.E., Goss, W.M., Winnberg, A., & Habing, H.J. 1977, A&A, 61, 261

Matthews, H.E., & Spoelestra, T.A.T. 1983, A&A, 126, 433

Matthews, N., Andersson, M., Macdonald, G.H. 1986, A&A, 155, 99

McKee, C. 1999, The Origin of Stars and Planetary Systems, eds. Charles J. Lada and Nikolaos D. Kylafis (Kluwer Academic Publishers), 29

Mestel, L., & Spitzer, L., Jr. 1956, Mon. Not. R. Astr. Soc., 116, 103

Mouschovias, T.Ch. 1987, Physical Processes in Interstellar Clouds, eds. G. Morfill and M. Scholer (Dordrecht: Reidel), 491

Mouchovias, T.Ch., & Spitzer, L., Jr. 1976, ApJ, 210 326

Mueller, K.E., Shirley, Y.L., Evans, N.J. II, & Jacobson, H.R. 2002, ApJS, 143, 469

Muñoz, D.J., Mardones, D., Garay, G., Rebolledo, D., Brooks, K., & Bontemps, S. 2007, ApJ, 668, 906

Neckel, T. 1978, A&A, 69, 51

Odenwald, S.F., & Schwartz, P.R. 1993, ApJ, 405, 706

Odenwald, S., Shivanandan, K., Campbell, M., Fazio, G., Schwartz, P., & Mosely, H. 1986, ApJ, 306, 122

Paleologou, E.V., & Mouschovias, T.Ch. 1983, ApJ, 275, 838

Panagia, N. 1973, AJ, 78, 929

- Parker, E.N. 1983, *SciAm*, 249, 44
- Persi, P., Tapia, M., & Roth, M. 2000, *A&A*, 357, 1020
- Piepenbrink, A., & Wendker, H.J. 1988, *A&A*, 191, 313
- Piddington, J.H., & Minnett, H.C. 1952, *AuSRA*, 5, 17
- Reifenstein, E.C., III, Wilson, T.L., Burke, B.F., Mezger, P.G., & Altenhoff, W.J. 1970, *A&A*, 4, 357
- Roberts, D.A., Crutcher, R.M., Troland, T.H., & Goss, W.M. 1993, *ApJ*, 412, 675
- Roberts, D.A., Crutcher, R.M., & Troland, T.H. 1995, *ApJ*, 442, 208
- Rodriguez, L.F., Cantó, J., & Moran, J.M. 1982, *ApJ*, 255, 103
- Rodriguez, L.F., Cantó, J., & Moran, J.M. 1988, *ApJ*, 333, 801
- Sandell, G. 1999, *A&A*, 343, 281
- Sarma, A.P., Troland, T.H., Roberts, D.A., & Crutcher, R.M. 2000, *ApJ*, 533, 271
- Sault, R.J., Teuben, P.J., & Wright, M.C.H. 1995, *ASPC*, 77, 433
- Schneider, N., Bontemps, S., Simon, R., Jakob, H., Motte, F., Miller, M., Kramer, C., & Stutzki, J. 2006, *A&A*, 458, 855
- Sekimoto, Y., Matsuzaki, K., Kamae, T., Tatematsu, K., Yamamoto, S., Umemoto, T. 2000, *PASJ*, 52, L31
- Sellgren, Tokunaga, & Nakada 1990
- Shepherd, D.S., Churchwell, E., & Wilner, D.J. 1997, *ApJ*, 482, 355
- Shirley, Y. L., Evans, N.J., II, Young, K.E., Knez, C., & Jaffe, D.T. 2003, *ApJS*, 149, 375
- Shu, F.H., Adams, F.C., & Lizano, S. 1987, *ARA&A*, 25, 23
- Shull, J.M. 1980, *ApJ*, 238, 860
- Spitzer, L., Jr. 1978, *Physical Processes in the Interstellar Medium* (New York: Wiley)



Troland, T.H., Crutcher, R.M., Goodman, A.A., Heiles, C., Kazes, I., & Myers, P.C. 1996, ApJ, 471, 302

Turner, D.G., & Forbes, D. 1982, PASP, 94, 789

Vacca, W.D., Garmany, C.D., & Shull, J.M. 1996, ApJ, 460, 914

Viti, S., Harquist, T.W., & Myers, P.C. 2006 Ap&SS, 302, 109

“The Very Large Array Observational Status Summary,” 2007, eds. J.S. Ulvestad, R.A. Perley, & G.B. Taylor,  
<http://www.vla.nrao.edu/astro/guides/vlas/current/>

Wendker, H.J., Higgs, L.A., & Landecker, T.L. 1991, A&A, 241, 551

Wolkovitch, D., Langer, W.D., Goldsmith, P.F., & Heyer, M. 1997, ApJ 477, 271

## Vita

### Biographical Information

Name: Elizabeth Ann Mayo  
Date of Birth: September 14<sup>th</sup>, 1976  
Place of Birth: Parkersburg, West Virginia

### Professional Preparation

West Virginia University	Physics	B.S.	1998
University of Kentucky	Physics	M.S.	2003

### Appointments

2006-Present	Planetarium Manager, Astronomy Educator SC State University, Orangeburg, SC
2006-Present	Instructor, Dept. of Biological and Physical Sciences SC State University, Orangeburg, SC
2000-2005	Research Assistant, Radio Astronomy Group, Dept. of Physics and Astronomy, University of Kentucky, Lexington, KY
Fall 1998, 2000-2002	Introductory Physics Graduate Teaching Assistant, Dept. of Physics and Astronomy, University of Kentucky, Lexington, KY

### Scholastic and Professional Honors

Recipient, Mountaineer Award, West Virginia University, 1994

Recipient, NASA Space Grant, West Virginia Space Grant Consortium, 1997

Outstanding Graduating Senior, Eberly College of Arts and Sciences, West Virginia University, 1998

Recipient, Graduate Assistance in Areas of National Need (GAANN) Fellowship, Department of Physics and Astronomy, University of Kentucky, 2000-2002

Recipient, NASA Space Grant, Kentucky Space Grant Consortium, 2002-2005

### Synergistic Activities

Manager of the NASA Educational Resource Center on the Campus of SC State University, Present.

Outreach Educator at the Living Arts and Science Center, Lexington, KY specializing in Star Lab Planetarium presentations for K-6 grades, 2004-2005.

Volunteer and Mentor for the Girls in Science Program at the University of Kentucky, 2004-2005.

### Relevant Publications

E.A. Mayo, A.P. Sarma, T.H. Troland; 2004; "VLA Zeeman Observations of the NGC 6334 Complex," *Bulletin of the American Astronomical Society*, v. 36, p. 771.

[2004AAS...205.9907M](#)

E.A. Mayo, A.P. Sarma, T.H. Troland, N.P. Abel; 2004; "VLA OH Zeeman Observations of the NGC 6334 Complex Source A," *Bulletin of the American Astronomical Society*, v. 36, p. 1507.

[2004AAS...204.6113M](#)

### Other Publications

Elizabeth Mayo, David Lederman, "Magnetoelastic Properties of Magnetic Thin Films Using the Magneto-optic Kerr Effect," *American Physical Society, Annual March Meeting, March 16-20, 1998 Los Angeles, Ca*, **1381.32**.

[1998APS..MARI38132M](#)

M. M. Schwickert, R. Coehoorn, M. A. Tomaz, D. Lederman, E. Mayo, W. L. O'Brien, Tao Lin, and G. R. Harp, "Magnetic Moments, Coupling, and Interface Interdiffusion in Fe/V(001) Multilayers," *Phys. Rev. B* **57**, 13681 (1998).

[1998PhRvB..5713681S](#)

M. A. Tomaz, E. Mayo, D. Lederman, E. Hallin, T. K. Sham, W. L. O'Brien, and G.R. Harp, "Magnetic Properties of Co/Rh (001) Multilayers Studied by X-ray Magnetic Circular Dichroism," *Phys. Rev. B* **58**, 11493 (1998).

[1998PhRvB..5811493T](#)

M. A. Tomaz, G. R. Harp, E. Mayo, D. Lederman, R. Wu, and W. L. O'Brien, "Structural and Magnetic Properties of Fe/Rh (001) Sputter Deposited Multilayers," *J. Vac. Sci. Technol. A* **16**, 1336 (1998).

[1998JVST...16.1336T](#)

M. A. Tomaz, G. R. Harp, D. Lederman, E. Mayo, and W. L. O'Brien, "Fe/Rh (100) Multilayer Magnetism Probed by XMCD," *Phys. Rev. B* **56**, 5474 (1997).

[1997PhRvB..56.5474T](#)

---

Elizabeth A. Mayo